Journal of Materials Chemistry B

ROYAL SOCIETY OF CHEMISTRY

PAPER

View Article Online
View Journal | View Issue

Cite this: J. Mater. Chem. B, 2025, 13, 15322

CD44 and mitochondria dual-targeted polydopamine nanoplatform for combined chemotherapy, photothermal ablation, and immunogenic cell death induction in liver cancer

Haizhou Qiu, Kunlin Chen, Yiwen Qiu, Yi Yang, Tao Wang, Li Jiang* and Wentao Wang *

Hepatocellular carcinoma (HCC) is a highly aggressive malignancy characterized by inadequate drug delivery to tumor sites, insufficient immune activation, and poor response to conventional monotherapies. To overcome these limitations, we developed a pH and near-infrared (NIR) responsive nanoplatform (DOX@MPDA-TPP@HA) by encapsulating doxorubicin (DOX) into mesoporous polydopamine (MPDA) nanoparticles functionalized with triphenylphosphonium (TPP) and hyaluronic acid (HA) to achieve mitochondrial and CD44 dual-targeting. This system enables combined chemotherapy and photothermal therapy, while simultaneously promoting immunogenic cell death and enhancing antitumor immunity. *In vitro* and *in vivo* experiments demonstrated that the nanoplatform exhibits acid and NIR-triggered drug release, efficient photothermal conversion, and enhanced cellular uptake in tumor cells. Treatment significantly increased calreticulin exposure and high-mobility group box 1 (HMGB1) release, both recognized as hallmarks of immunogenic cell death. Flow cytometry revealed a marked increase in the maturation of $CD11c^+CD80^+CD86^+$ dendritic cells in tumor-draining lymph nodes, elevated intratumoral $CD8^+$ cytotoxic T lymphocyte infiltration, and a reduction in $CD4^+Foxp3^+$ regulatory T cells. Enzyme-linked immunosorbent assay (ELISA) confirmed the elevated secretion of proinflammatory cytokines including interleukin-6, interleukin-12, tumor necrosis factor-alpha, and interferon-gamma, suggesting immune reprogramming of the tumor microenvironment. Collectively, these results demonstrate that DOX@MPDA-TPP@HA effectively integrates chemotherapy, photothermal ablation, and immune modulation, offering a promising therapeutic strategy for the treatment of hepatocellular carcinoma.

Received 22nd August 2025,
Accepted 4th November 2025

DOI: 10.1039/d5tb01901j

rsc.li/materials-b

1. Introduction

Hepatocellular carcinoma (HCC) ranks as the third leading cause of cancer-related death worldwide, with rising incidence largely driven by chronic hepatitis B or C infection, alcohol-associated liver disease, and metabolic dysfunction–associated steatotic liver disease.[1] HCC is characterized by aggressive progression, vascular invasion, early metastasis, and poor response to conventional therapies, leading to a five-year survival rate below 20%.[2] While surgical resection and locoregional treatments benefit early-stage patients, cytotoxic chemotherapy (chemo) may be considered when curative approaches are not feasible.[3] However, its efficacy is limited by poor tumor selectivity, systemic toxicities such as cardiotoxicity and myelosuppression, rapid clearance, and multidrug resistance.[4] The complex tumor microenvironment of the liver further restricts drug penetration and therapeutic outcomes.[5] These limitations motivate the development of advanced drug-delivery systems that enhance tumor targeting, improve therapeutic efficacy, and potentially engage antitumor immunity.

Nanoparticle-based drug carriers are designed to enhance intratumoral drug exposure. By increasing tumor accumulation and enabling stimulus-responsive, on-demand release, these carriers can reduce systemic exposure and associated toxicities. Among these carriers, mesoporous polydopamine (MPDA) nanoparticles offer excellent biocompatibility, efficient near-infrared (NIR) photothermal conversion, versatile surface chemistry for ligand conjugation, and high drug-loading capacity.[6] Polydopamine forms *via* dopamine self-polymerization under alkaline conditions and presents catechol and amine (and imine) groups that enable π–π stacking and electrostatic loading, while also facilitating ligand attachment.[7] Recent studies indicate that

Division of Liver Surgery, Department of General Surgery, West China Hospital of Sichuan University, Chengdu, Sichuan Province, 610041, China.
E-mail: jlhx339@163.com, wwtdoctor02@163.com

MPDA can accommodate diverse therapeutic cargo across solid tumor models, including polydopamine-based targeted chemo–photothermal systems.[8]

Tian *et al.* incorporated the NIR dye IR-780 into MPDA to enable imaging-guided photothermal therapy (PTT) and photodynamic therapy (PDT), reporting substantial tumor suppression with elevated immunogenic cell death (ICD) hallmarks in 4T1 breast cancer.[9] Xu *et al.* encapsulated doxorubicin in MPDA and added a fucoidan–disulfide shell to achieve pH/GSH-responsive release; with NIR-assisted PTT, the nanoplatforms produced stronger growth inhibition in HCT-116 colorectal cancer cells.[10] Wang *et al.* loaded cisplatin into MPDA, capped the mesopores with MnO_2, and decorated the surface with a human epidermal growth factor receptor 2 (HER2) affibody for targeting. The construct was magnetic resonance imaging (MRI)-traceable and sensitized chemoradiotherapy in HER2-overexpressing ovarian cancer.[11]

In view of MPDA's selection as the carrier and its demonstrated payload versatility, the therapeutic concept centers on doxorubicin (DOX), triphenylphosphonium (TPP^+)-mediated mitochondrial delivery, and NIR-activated PTT. DOX exerts cytotoxicity *via* DNA intercalation, topoisomerase II inhibition, and reactive oxygen species (ROS) generation; it can also elicit ICD characterized by calreticulin (CRT) exposure and adenosine triphosphate (ATP)/high-mobility group box 1 (HMGB1) release, which promote dendritic-cell maturation and CTL priming.[12–15] Mitochondria orchestrate DOX- and ROS-related apoptotic pathways; enrichment of drug at this organelle is therefore expected to improve effectiveness. Mitochondrial localization is achieved with the lipophilic cation TPP^+, which accumulates in response to the mitochondrial membrane potential ($\Delta\Psi_m$) and thereby improves subcellular delivery.[16] PTT provides a minimally invasive modality for local ablation. MPDA exhibits strong NIR absorption and high photothermal conversion efficiency, enabling direct thermal injury while enhancing drug release and cellular uptake.[6,17] The tissue penetration of NIR light is limited, which attenuates efficacy in deep lesions.[18] Accordingly, chemotherapy combined with PTT (chemoPTT) is frequently employed to achieve synergistic cytotoxicity and may further augment ICD-associated responses.[19] As further support, recent combination-therapy studies, together with reviews of supramolecular nanoplatforms that enable versatile surface functionalization and multifunctional assembly, support this strategy.[20,21]

CD44 is a hyaluronan receptor frequently upregulated in HCC that mediates HA-dependent endocytosis; therefore, HA decoration is expected to enhance cellular uptake.[22,23] In this study, as illustrated in Scheme 1, a mitochondria-targeted MPDA nanoplatform (DOX@MPDA-TPP@HA) was developed for HCC. The nanoplatform comprises DOX-loaded MPDA nanoparticles functionalized with hyaluronic acid (HA) and TPP^+ to enable CD44-mediated uptake and mitochondrial localization. After cellular uptake, NIR irradiation drives photothermal conversion by the MPDA core, thereby promoting DOX release within the acidic tumor microenvironment and complementing chemotherapeutic activity. The combined chemo-PTT

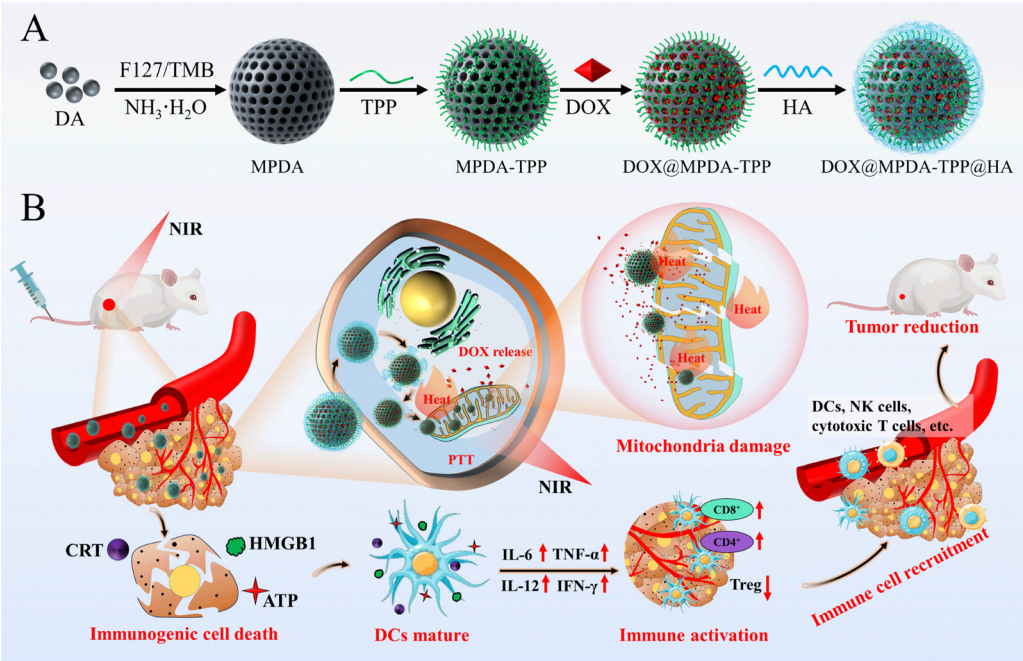

Scheme 1 Schematic illustration of the mitochondria-targeted MPDA-based nanoplatform (DOX@MPDA-TPP@HA) for chemo-PTT therapy of HCC with ICD-linked immune activation. (A) Assembly of the nanoplatform: MPDA is prepared by dopamine polymerization (F127/TMB, $NH_3{\cdot}H_2O$), followed by sequential TPP^+ grafting, DOX loading, and HA coating for CD44 targeting. (B) Proposed therapeutic mechanism: After HA–CD44–mediated endocytosis by CD44-overexpressing HCC cells, NIR irradiation triggers MPDA photothermal heating and DOX release; mitochondrial accumulation causes mitochondrial damage. Chemo-PTT synergy induces ICD (CRT, ATP, HMGB1), drives immune activation, and suppresses tumor growth.

approach intensifies tumor-cell killing and yields ICD hallmarks (CRT exposure and ATP/HMGB1 release), which can promote dendritic-cell maturation and T-cell infiltration within the tumor microenvironment. Together, these features provide a mechanistic basis for improved therapeutic performance over chemotherapy alone.

2. Materials and methods

2.1. Materials

Dopamine (DA), (3-carboxypropyl) triphenylphosphonium bromide (TPP-COOH), sodium hyaluronate (HA), Pluronic F127 (F127), aqueous ammonia, *N*,*N*-dimethylformamide (DMF), 1-ethyl-3-(3-dimethylaminopropyl)carbodiimide (EDC), *N*-hydroxysuccinimide (NHS), doxorubicin (DOX), ethanol, 2′,7′-dichlorodihydrofluorescein diacetate (DCFH-DA), 1,3,5-trimethylbenzene (TMB), and 4′,6-diamidino-2-phenylindole (DAPI) were purchased from Aladdin Reagent Co., Ltd (Shanghai, China). Phosphate-buffered saline (PBS), fetal bovine serum (FBS), penicillin–streptomycin, Cell Counting Kit-8 (CCK-8), JC-1 mitochondrial membrane potential assay kit, Annexin V-FITC/PI apoptosis detection kit, and MitoTracker Green were obtained from Beyotime Biotechnology (Shanghai, China). Antibodies including anti-CD11c-FITC, anti-CD80-PE, anti-CD86-APC, anti-CD3-FITC, anti-CD4-APC, anti-CD8-PE, and anti-Foxp3-PE were supplied by Elabscience Biotechnology Co., Ltd (Wuhan, China). Unless otherwise specified, all reagents were of analytical grade. Unless otherwise specified, PBS refers to 1× PBS.

2.2. Synthesis of MPDA-based nanoplatforms (MPDA, MPDA-TPP, DOX@MPDA-TPP, and DOX@MPDA-TPP@HA)

To prepare MPDA, deionized water (5 mL) and ethanol (5 mL) were added to a round-bottom flask, followed by F127 (100 mg), dopamine (DA, 150 mg), and TMB (0.2 mL). TMB served as a hydrophobic porogen that swelled F127 micelles, thereby templating mesopores in MPDA. Residual TMB was removed during washing. The mixture was ultrasonicated for 2 min to form a milky emulsion. Aqueous ammonia (2 M, 0.375 mL) was then introduced, and the reaction was allowed to proceed for 2 h at room temperature. The precipitate was collected by centrifugation (8500 rpm, 8 min), washed three times with water and ethanol, and redispersed in ethanol to afford MPDA.

To prepare MPDA-TPP, TPP-COOH (100 mg) was dissolved in DMF and activated with EDC/NHS for 2 h; an MPDA suspension (100 mg, in DMF/ethanol) was then added dropwise to the activated solution and stirred overnight. The solid was collected by centrifugation and washed repeatedly with water and ethanol to remove residual reagents, and finally redispersed in ethanol to yield MPDA-TPP.

To prepare DOX@MPDA-TPP, MPDA-TPP (30 mg) and DOX(10 mg) were dispersed in DMF and stirred overnight. The product was isolated by centrifugation, thoroughly washed to remove free DOX, and redispersed to yield DOX@MPDA-TPP.

To prepare DOX@MPDA-TPP@HA, a solution of hyaluronic acid (HA, 5 mg in PBS, pH 7.4) was added to a suspension of DOX@MPDA-TPP (20 mg) and stirred overnight at room temperature. The resulting dispersion was collected by centrifugation, washed three times with PBS (pH 7.4) to remove unbound HA, and finally redispersed in PBS (pH 7.4) to yield DOX@MPDA-TPP@HA.

Unless otherwise stated, procedures were carried out at room temperature. DOX-related operations were performed under light protection.

2.3. Characterization of MPDA-based nanoplatforms

2.3.1. Physicochemical characterization. Transmission electron microscopy (TEM) was used to assess particle morphology and core size: 10 μL of nanoparticle dispersion was dropped onto a carbon-coated copper grid, dried in a vacuum oven at 50 °C for 24 h, and imaged by TEM (JEOL JEM-2100, 200 kV; JEOL Ltd, Japan). Dynamic light scattering (DLS) and laser Doppler electrophoresis (Zetasizer Nano ZS; Malvern Panalytical, UK) were performed to determine the hydrodynamic size distribution, polydispersity index (PDI), and zeta potential of aqueous dispersions. Fourier-transform infrared (FT-IR) spectroscopy (Nicolet iS10; Thermo Fisher Scientific, USA, KBr pellet method) was used to verify surface conjugation (*e.g.*, TPP on MPDA) by comparing characteristic vibrational bands among MPDA, MPDA-TPP, DOX@MPDA-TPP, and DOX@MPDA-TPP@HA. Nitrogen adsorption–desorption isotherms were recorded at liquid-nitrogen temperature (−196 °C) on an ASAP 2020 surface area analyzer (Micromeritics, USA); the specific surface area and mesoporous parameters were obtained from BET analysis of the isotherms. UV-Vis spectra (UV-2600; Shimadzu, Japan, 200–900 nm) were recorded to determine absorbance at 808 nm (A_{808}); for DOX-containing samples, DOX was quantified at 480 nm.

2.3.2. Drug loading, encapsulation efficiency, and *in vitro* release. A calibration curve for DOX was established by dissolving DOX (10 mg) in deionized water (10 mL) to obtain a 1 mg mL^{-1} stock, followed by dilution to 40, 20, 10, 5, 2, and 1 μg mL^{-1}. UV-Vis spectra (200–900 nm) were recorded to determine A_{480}; and linear regression of A_{480} *versus* concentration was used for quantification. For loading, MPDA-TPP was incubated with DOX and then centrifuged; the supernatant A_{480} gave the mass of free DOX *via* the calibration curve. DOX in nanoparticles was calculated as (input DOX – free DOX). Loading capacity (LC) and encapsulation efficiency (EE) were calculated according to the following eqn (1) and (2):

$$\mathrm{LC} = \frac{\text{Drug mass within nanoparticles}}{\text{Total mass of nanoparticles}} \times 100\% \quad (1)$$

$$\mathrm{EE} = \frac{\text{Drug mass within nanoparticles}}{\text{Mass of drug input}} \times 100\% \quad (2)$$

In vitro release from DOX@MPDA-TPP@HA was evaluated at 37 °C using a centrifugation/sampling method. Dispersions (1 mL) were prepared in PBS (pH 7.4) and in PBS (pH 6.5) containing hyaluronidase (HAase). At predefined time points, samples received 808 nm irradiation (1.0 W cm^{-2}, 5 min) as indicated, were centrifuged, and supernatants were analyzed at 480 nm to obtain DOX concentration from the calibration

curve. After measurement, supernatants were returned to the original tubes to maintain constant volume; cumulative release (%) was calculated relative to the total DOX in the nanoparticles. Experiments were performed in triplicate (n = 3) and reported as mean ± SD. Note: ultrafiltration devices were not used in loading or release experiments. Free DOX was quantified directly from centrifuged supernatants using the 480 nm calibration curve.

2.3.3. Photothermal performance and conversion efficiency. For concentration dependence, DOX@MPDA-TPP@HA dispersions (50, 100, 200, 400 μg mL^{-1}; 1 mL each in 1.5 mL microtubes) and deionized water (control) were irradiated with an 808 nm laser (MDL-III-808; CNI, China) at 1.0 W cm^{-2}; temperature was recorded at every 1 min. For power dependence, a 200 μg mL^{-1} dispersion was irradiated at 0.5, 1.0, and 2.0 W cm^{-2} and the temperature rise was monitored. Photothermal cycling stability was evaluated with 1 mL of a 1 mg mL^{-1} dispersion under 808 nm irradiation at 1.0 W cm^{-2} for four on/off cycles (10 min on followed by natural cooling to the initial temperature), recording temperature every 1 min.

The photothermal conversion efficiency (η) was calculated as eqn (3):

$$\eta = \frac{hS\Delta T_{max} - Q_{dis}}{I(1 - 10^{-A_{808}})} \quad (3)$$

where h is the heat-transfer coefficient, S is the container surface area, ΔT_{max} is the maximum temperature rise (sample minus ambient), Q_{dis} is the heat associated with light absorbed by the solvent, I is the incident laser power (808 nm), and A_{808} is the absorbance at 808 nm. The quantity hS was determined from eqn (4) by cooling-curve analysis.

The product hS was obtained from eqn (4):

$$\tau_s = \frac{m_D C_D}{hS} \quad (4)$$

where τ_s is the time constant from the cooling-curve fit, and m_D and C_D are the mass and specific heat capacity of the solvent, respectively. During post-irradiation cooling, the dimensionless temperature θ was defined as $(T - T_{env})/(T_{max} - T_{env})$. τ_s was obtained from a linear fit of $-\ln(\theta)$ *versus* time; $hS = m_D C_D/\tau_s$ and was then substituted into eqn (3) to evaluate η.

2.3.4. Hemocompatibility (hemolysis assay). Hemocompatibility was assessed using a hemolysis assay with human red blood cells (RBCs). Briefly, whole blood (0.5 mL; containing ~0.4 mL packed cells) was centrifuged to remove plasma, and RBCs were washed repeatedly with 0.9% NaCl until the supernatant was clear. The cells were then resuspended in 0.9% NaCl to 4 mL to obtain a 1 : 10 dilution (10% v/v RBC suspension). Test dispersions of DOX@MPDA-TPP@HA at various concentrations were prepared in microcentrifuge tubes; to each tube, 0.5 mL of the diluted RBC suspension was added and the mixtures were incubated at 37 °C for 2 h. Samples were centrifuged at 750 × g for 5 min, and the absorbance of the supernatant at 540 nm (A_{540}) was recorded using a UV-Vis spectrophotometer. Negative and positive controls were 0.9% NaCl and deionized water, respectively. The hemolysis percentage was calculated as eqn (5):

$$\text{Hemolysis (\%)} = \frac{A_{sample} - A_{negativecontrol}}{A_{positivecontrol} - A_{negativecontrol}} \times 100\% \quad (5)$$

Results were reported as mean ± SD (n = 3). A hemolysis rate below 5% was considered acceptable for hemocompatibility.

2.4. *In vitro* cell assays on Huh7 and L929 cells

2.4.1. Cell culture and treatment groups. Human hepatocellular carcinoma Huh-7 (Cat. iCell-h107) and mouse fibroblast L929 (Cat. iCell-m026) cell lines were obtained from Cellverse Co., Ltd (Shanghai, China). Cells were cultured in DMEM supplemented with 10% FBS and 1% penicillin–streptomycin at 37 °C in a humidified incubator with 5% CO_2. Unless otherwise specified, *in vitro* experiments employed the following groups: control, MPDA-TPP@HA, MPDA-TPP@HA + NIR, DOX, DOX@MPDA-TPP@HA, and DOX@MPDA-TPP@HA + NIR. For NIR irradiation, cultures were exposed to an 808 nm laser at 1.0 W cm^{-2} for 5 min after the indicated incubation period; sham controls underwent identical handling without laser exposure.

2.4.2. Cellular uptake and mitochondrial colocalization. Huh7 cells were seeded in 24-well plates and allowed to adhere for 24 h, then incubated with DOX@MPDA-TPP or DOX@MPDA-TPP@HA for 2 h or 4 h. After incubation, cultures were rinsed with PBS (pH 7.4) to remove unbound material and imaged by CLSM (LSM 510, Carl Zeiss, Germany) using intrinsic DOX fluorescence (red channel) under identical acquisition settings across groups. To compare HA-mediated uptake, a separate flow-cytometry assay was performed at 4 h with equal DOX-equivalent doses and without NIR irradiation. Groups included control, DOX@MPDA, DOX@MPDA-HA, DOX@MPDA-TPP, DOX@MPDA-TPP@HA, and the blocking conditions free HA + DOX@MPDA-TPP@HA and free HA + DOX@MPDA-TPP. For the blocking condition, cells were preincubated with free HA (0.5 mg mL^{-1}, 30 min, 37 °C) prior to exposure to the nanocarrier groups, then rinsed with PBS and replaced with fresh medium for uptake measurement. Uptake was quantified by flow cytometry as mean fluorescence intensity (MFI) in the DOX channel (≥10 000 events per sample; debris and doublets excluded by standard FSC/SSC gating).

For mitochondrial colocalization, Huh7 cells were incubated for 24 h with DOX@MPDA, DOX@MPDA-TPP, or DOX@MPDA-TPP@HA. Cells were then stained with MitoTracker Green (15 min at 37 °C, protected from light) and counterstained with DAPI (5 min), washed three times with PBS (pH 7.4) to remove excess dye, and imaged by CLSM.

2.4.3. Cytotoxicity and *in vitro* antitumor activity. For biocompatibility, L929 cells were seeded in flat-bottom 96-well plates at 1.0 × 10^4 cells per well in 100 μL complete DMEM (10% FBS, 1% penicillin–streptomycin) and allowed to adhere for 24 h (37 °C, 5% CO_2). Medium was replaced with serum-free DMEM containing MPDA-based dispersions at 25, 50, 100, 200, or 400 μg mL^{-1} (100 μL per well) and cells were incubated for 24 h. Wells with serum-free DMEM only served as untreated

controls. After treatment, CCK-8 reagent (10 μL per well) was added and plates were incubated 3 h in the dark at 37 °C. Absorbance at 450 nm was read on a microplate reader (SpectraMax M5, Molecular Device, United States s). Cell viability (%) was calculated as eqn (6):

$$\text{Cell viability } (\%) = \frac{A_{\text{experimental group}} - A_{\text{blank group}}}{A_{\text{control group}} - A_{\text{blank group}}} \times 100\% \quad (6)$$

where $A_{\text{control group}}$ and $A_{\text{experimental group}}$ refer to absorbance of the treated (experimental) wells and absorbance of the untreated control wells, respectively; $A_{\text{blank group}}$ is the absorbance of the blank wells (medium + CCK-8).

To evaluate the *in vitro* antitumor effect of DOX@MPDA-TPP@HA, Huh7 cells were seeded in 96-well plates (1.0×10^4 cells per well; 100 μL complete DMEM) and allowed to adhere for 24 h. Cells were then treated at the indicated concentrations with six groups: control, MPDA-TPP@HA, MPDA-TPP@HA + NIR, DOX, DOX@MPDA-TPP@HA, and DOX@MPDA-TPP@HA + NIR. After 8 h incubation, NIR-designated wells were irradiated at 808 nm, 1.0 W cm^{-2} for 5 min; sham controls underwent identical handling without laser exposure. Cultures were further incubated to 24 h total from treatment onset, and cell viability was determined by CCK-8 assay, as described previously (eqn (6)).

For live/dead staining, Huh7 cells were seeded on glass-bottom confocal dishes (35-mm dish, 14-mm imaging well) at 1.5×10^5 cells per dish in 2 mL complete DMEM and allowed to adhere for 24 h (37 °C, 5% CO_2). Cells then received the six treatment groups at the indicated concentrations (control, MPDA-TPP@HA, MPDA-TPP@HA + NIR, DOX, DOX@MPDA-TPP@HA, DOX@MPDA-TPP@HA + NIR). After 8 h incubation, NIR-designated dishes were irradiated (808 nm, 1.0 W cm^{-2}, 5 min); sham controls were handled identically without laser. Cultures were returned to the incubator and maintained until 24 h from treatment onset. For staining, media were replaced with phenol-red–free DMEM containing Calcein AM 2 μM and propidium iodide (PI) 2 μg mL^{-1}. Dishes were incubated 15 min at room temperature in the dark, then gently rinsed twice with PBS (pH 7.4). Imaging was performed on a CLSM (LSM 510, Carl Zeiss, Germany).

For apoptosis analysis, cells from each group were harvested and adjusted to 1×10^6 cells per mL; 200 μL aliquots were centrifuged (1000 rpm, 5 min, 4 °C) and washed twice with pre-cooled PBS (pH 7.4, 1 mL). Pellets were resuspended in 100 μL binding buffer, followed by addition of Annexin V-FITC (2 μL, 20 μg mL^{-1}) with gentle mixing and incubation 15 min on ice in the dark. Samples were transferred to flow tubes, supplemented with 400 μL PBS (pH 7.4), and 1 μL PI (50 μg mL^{-1}) was added immediately before acquisition. Flow cytometry was performed on a flow cytometer (FACS Calibur, BD Biosciences, USA) using appropriate filters for FITC and PI; fluorescence compensation was set using single-stained controls.

2.4.4. Intracellular ROS and mitochondrial membrane potential ($\Delta\Psi_m$). Intracellular ROS (DCFH-DA). Huh7 cells were seeded in 24-well plates and allowed to adhere for 24 h, then treated with the six groups at the indicated concentrations (control, MPDA-TPP@HA, MPDA-TPP@HA + NIR, DOX, DOX@MPDA-TPP@HA, DOX@MPDA-TPP@HA + NIR). After 8 h, NIR-designated wells were irradiated (808 nm, 1.0 W cm^{-2}, 5 min) and cultures were returned to the incubator until 24 h from treatment onset. For ROS labeling, cells were incubated with DCFH-DA 10 μM in pre-warmed, phenol-red-free medium for 30 min at 37 °C in the dark, then rinsed with PBS (pH 7.4) and imaged by CLSM. Mean fluorescence intensity (MFI) was quantified per field/ROI using standard image-analysis software with identical thresholding across groups. In parallel, cells were harvested and analyzed by flow cytometry in the FITC channel.

Mitochondrial membrane potential (JC-1). Huh7 cells were seeded on glass-bottom confocal dishes and subjected to the same treatments (including NIR where applicable). At 24 h from treatment onset, cells were stained with JC-1 (5 μg mL^{-1}) for 20 min at 37 °C in the dark, rinsed with PBS (pH 7.4), and imaged by CLSM. JC-1 aggregates were collected in the red channel, and monomers in the green channel. $\Delta\Psi_m$ was expressed as the red/green fluorescence ratio per cell/ROI.

2.4.5. ICD hallmarks and western blot. Huh7 cells were seeded in 24-well plates and allowed to adhere for 24 h, then treated at the indicated concentrations with six groups: control, MPDA-TPP@HA, MPDA-TPP@HA + NIR, DOX, DOX@MPDA-TPP@HA, and DOX@MPDA-TPP@HA + NIR. After 8 h, NIR-designated wells were irradiated (808 nm, 1.0 W cm^{-2}, 5 min) and cultures were maintained to 24 h from treatment onset for ICD readouts. At 24 h, culture supernatants were collected, clarified (12 000×*g*, 5 min), and assayed with a luminescence-based ATP kit on a microplate reader.

For CRT surface exposure, monolayers were rinsed with PBS (pH 7.4) and fixed with 4% paraformaldehyde (10 min, RT). Without permeabilization, cells were blocked in 3% BSA/PBS (pH 7.4) for 30 min and incubated with anti- CRT primary antibody (1 : 200, 1 h, RT). After PBS (pH 7.4) washes, a fluorophore-conjugated secondary antibody (1 : 500, 1 h, RT) was applied; nuclei were counterstained with DAPI (1 μg mL^{-1}, 5–10 min). Imaging was performed on a CLSM under fixed acquisition settings. Quantification reported % CRT-positive cells and mean fluorescence intensity (MFI) from ≥3 random fields per well; isotype controls were included.

For HMGB1 release, cells were fixed (4% paraformaldehyde, 10–15 min, RT), permeabilized (0.1% Triton X-100, 10 min), blocked (3% BSA, 30 min), and incubated with anti-HMGB1 primary antibody (overnight, 4 °C), followed by a fluorophore-conjugated secondary (1 : 500, 1 h, RT) and DAPI. CLSM imaging was performed as above, and HMGB1 redistribution was quantified as the nuclear-to-cytoplasmic fluorescence ratio per ROI; primary-antibody–omission controls were included.

For western blotting, treated cells were lysed on ice in RIPA buffer (30 min). Protein concentrations were determined by BCA assay. Equal protein (20 μg) was resolved by SDS-PAGE (10–12%) and transferred to PVDF membranes. Membranes were blocked (5% nonfat milk, 1 h, RT), probed with anti-CRT, anti-HMGB1, and anti-GAPDH (overnight, 4 °C), and then with HRP-conjugated secondaries (2 h, RT). Bands were visualized

using an ECL system (FluorChemR, Protein Simple, USA) and quantified by densitometry (ImageJ), normalizing targets to GAPDH.

2.5. *In vivo* studies

2.5.1. Tumor model establishment. Female BALB/c mice (6–8 weeks) were used for all *in vivo* experiments. All procedures complied with institutional guidelines and were approved by the laborator animal welfare and ethics committee of West China Hospital of Sichuan University (no. 2021275A). Mice were maintained under SPF conditions with *ad libitum* access to food and water. Subcutaneous xenografts were established by injecting Huh7 cells (1×10^7 cells in 100 μL PBS, pH 7.4) into the right flank; treatments were initiated when tumors reached $\sim$100 mm^3.

2.5.2. *In vivo* biodistribution and *ex vivo* imaging. Tumor-bearing mice received a single tail-vein injection of DOX@MPDA-TPP or DOX@MPDA-TPP@HA at a doxorubicin-equivalent dose of 2.5 mg kg^{-1} (injection volume 200 μL). For imaging, mice were anesthetized with isoflurane (induction 3%, maintenance 1.5–2.0% in O_2) and placed prone on a 37 °C heated stage with a nose cone. Whole-body fluorescence was acquired at 2, 4, 8, 12, and 24 h post-injection using a small-animal imaging system (IVIS Lumina III, PerkinElmer, United States). Hair over the tumor region was removed 24 h prior to imaging to reduce light attenuation.

At 24 h, mice were euthanized; heart, liver, spleen, lung, kidney, and tumor were excised, gently rinsed in PBS (pH 7.4), blotted dry, and arranged in a Petri dish for *ex vivo* imaging using the same filter set and fixed exposure. Regions of interest (ROIs) were drawn over tumor or organs with a background ROI placed on a non-tissue area of the same image.

2.5.3. Antitumor efficacy *in vivo*. Mice were randomized into six groups: control (saline), MPDA-TPP@HA, MPDA-TPP@HA + NIR, DOX, DOX@MPDA-TPP@HA, and DOX@MPDA-TPP@HA + NIR (n = 6 per group). Nanoplatforms were administered intravenously at a doxorubicin-equivalent dose of 2.5 mg kg^{-1} every two days. For NIR groups, tumors were irradiated 12 h post-injection using an 808 nm diode laser (1.0 W cm^{-2}, 5 min; beam spot covering the entire tumor). Mice were anesthetized with isoflurane (induction 3%, maintenance 1.5–2.0% in O_2) and placed on a 37 °C heated stage.

Tumor length (L) and width (W) and body weight were recorded every 2 days. Tumor volume (V) was calculated as eqn (7):

$$V = \frac{L \times W^2}{2} \tag{7}$$

At study end, tumors and major organs were harvested. Tumor sections underwent H&E, TUNEL, and Ki-67 staining under identical staining and imaging settings across groups. Where indicated, DCFH-DA fluorescence was used to assess intratumoral ROS on tumor samples.

2.5.4. *In vivo* immune analyses. To evaluate ICD-linked markers and lymphocyte infiltration in tumors, excised tumors were fixed and sectioned. For CRT surface exposure, sections were processed without permeabilization; for HMGB1 redistribution and CD8/CD4 staining, sections were permeabilized (0.1% Triton X-100). After blocking (3% BSA/PBS), sections were incubated with primary antibodies to CRT, HMGB1, CD8, and CD4, followed by fluorophore-conjugated secondaries; nuclei were counterstained with DAPI. Images were acquired on a CLSM under standardized acquisition settings across groups.

To quantify dendritic-cell maturation in tumor-draining lymph nodes (TDLNs), inguinal nodes were mechanically dissociated through a 70-μm strainer into ice-cold PBS (pH 7.4) + 2% FBS; red cells were lysed as needed. Single-cell suspensions were stained with CD11c-FITC, CD80-PE, CD86-APC (± viability dye). Data were acquired on a flow cytometer with single-stain and fluorescence-minus-one controls for compensation and gating. Events were gated to exclude debris (FSC/SSC), doublets (FSC-A *vs.* FSC-H), and dead cells (viability dye), then analyzed for $CD11c^+$ cells co-expressing CD80 and/or CD86.

To characterize tumor-infiltrating T cells and regulatory T cells (Tregs), tumors were enzymatically and mechanically dissociated to single cells, filtered (70-μm), and stained with CD3-FITC, CD4-APC, CD8-PE. Within the $CD3^+$ gate, the proportions of $CD8^+$ and $CD4^+$ T cells were quantified. Tregs were identified by intracellular Foxp3-PE staining following fixation/permeabilization of $CD3^+CD4^+$ cells with a Foxp3 kit. Gating followed the same debris/doublet/dead-cell exclusion as above. Results were expressed as % $CD8^+$ and % $CD4^+$ within $CD3^+$, and % $Foxp3^+$ within $CD4^+$.

To profile the intratumoral cytokine milieu, tumors were homogenized in ice-cold PBS (pH 7.4) with protease inhibitors; supernatants were clarified by centrifugation and assayed for TNF-α, IL-6, IL-12, IFN-γ using ELISA kits (read on a microplate reader). Concentrations were normalized to total protein (BCA assay) and reported as pg mg^{-1} protein.

2.5.5. *In vivo* biosafety assessment. Healthy BALB/c mice received DOX@MPDA-TPP@HA *via* tail vein at a DOX-equivalent dose of 2.5 mg kg^{-1}; untreated mice served as controls. Cohorts were euthanized on day 1, day 7, and day 14. Under isoflurane anesthesia, retro-orbital blood ($\approx$ 200 μL) was collected into EDTA microtubes for hematology and into serum tubes for biochemistry. Serum was obtained by clotting (45 min, RT) and centrifugation (3000 rpm, 10 min). Hematology and serum chemistry (ALT, AST, ALP, BUN, creatinine; optional TBIL) were measured using commercial assay kits (Elabscience Biotechnology Co., Ltd, Wuhan, China).

Major organs (heart, liver, spleen, lung, kidney) were excised, rinsed in PBS (pH 7.4), and fixed in 10% neutral-buffered formalin (NBF) for 24 h, paraffin-embedded, sectioned (4 μm), and H&E stained.

2.6. Statistical analysis

Data are presented as mean ± standard deviation (SD). Unless otherwise specified, experiments were performed in triplicate. For comparisons involving more than two groups, one-way ANOVA followed by Tukey's *post hoc* test was applied; two-way ANOVA was used for longitudinal tumor-growth curves.

Statistical significance was denoted as ns (not significant), * $p < 0.05$, ** $p < 0.01$, and *** $p < 0.001$.

3. Results and discussion

3.1. Characterization of MPDA-based nanoplatforms

In this study, a hyaluronic acid–coated, mitochondria-targeted MPDA nanoplatform for HCC (DOX@MPDA-TPP@HA) was designed (Scheme 1) and validated by comprehensive physicochemical analyses (Fig. 1). Fig. 1A (TEM) shows uniform spherical MPDA with an average diameter of ~190 nm; radially oriented mesochannels are evident throughout the particles. Nitrogen adsorption–desorption (Fig. S1A and B) displays an IUPAC type IV isotherm with a BET surface area of 22.57 $m^2 g^{-1}$ and a pore-size distribution centered at 2–5 nm, a range suitable for small-molecule loading and diffusion. After TPP conjugation and DOX loading, TEM confirmed retention of spherical morphology (Fig. 1B and C), and DLS indicated minor shifts in hydrodynamic diameter relative to MPDA (Fig. 1F and G), suggesting that mesostructure and dispersibility were preserved during these steps. To improve interfacial properties and enable CD44-mediated uptake, the surface of DOX@MPDA-TPP was coated with HA, yielding DOX@MPDA-TPP@HA with intact morphology but smaller apparent surface pore openings than bare MPDA (Fig. 1D). The HA corona increased the hydrodynamic diameter to ~200 nm while maintaining a narrow distribution (Fig. 1H), indicative of good aqueous dispersion.

Chemical and interfacial readouts corroborated successful functionalization. FT-IR spectra supported TPP grafting onto MPDA, with MPDA-TPP exhibiting new bands at 689 and 740 cm^{-1} that are diagnostic of a monosubstituted phenyl ring (Fig. 1I). Interfacial charge evolved stepwise during assembly: the zeta potential shifted from −29.5 mV for MPDA to +15.5 mV after TPP conjugation, and to −21.2 mV following HA coating (Fig. 1J). This pattern is consistent with incorporation of cationic TPP followed by formation of an anionic HA corona, which is expected to attenuate nonspecific interactions while preserving CD44-mediated uptake. Dispersions remained colloidally stable over 7 days in PBS (pH 7.4) and in serum-containing medium, with essentially constant hydrodynamic size by DLS (Fig. 1K), and with PDI remaining low over 7 days in PBS (Table S1). Hemocompatibility testing showed <5% hemolysis even at 400 μg mL^{-1} (Fig. 1L).

MPDA-based nanoplatforms can load diverse therapeutics and imaging agents to enable combination regimens and stimulus-responsive delivery. For instance, Tian *et al.* incorporated the NIR dye IR-780 into MPDA (IR-780@MPDA) to achieve imaging-guided photothermal/photodynamic therapy and significant tumor suppression in a 4T1 breast-cancer model,

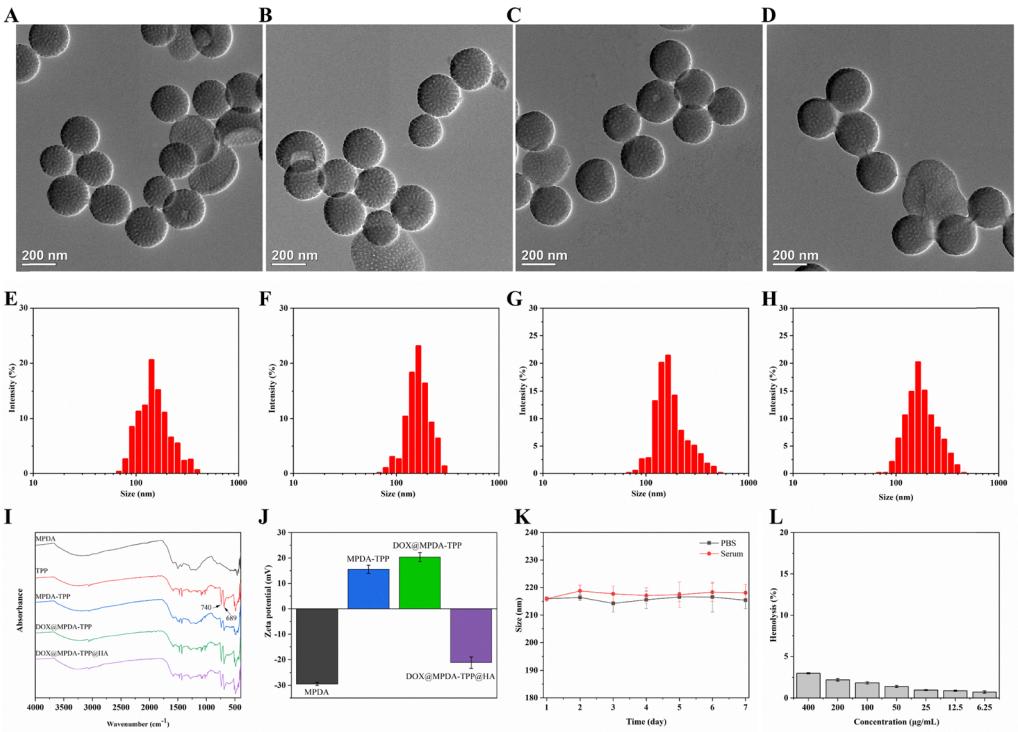

Fig. 1 Physicochemical characterization of MPDA-based nanoplatforms. Panels (A)–(D) refer to TEM images of MPDA (A), MPDA-TPP (B), DOX@MPDA-TPP (C), and DOX@MPDA-TPP@HA (D). Panels (F)–(H) refer to hydrodynamic size distributions of MPDA(E), MPDA-TPP (F), DOX@MPDA-TPP (G), and DOX@MPDA-TPP@HA (H). Panel (I) refer to FT-IR spectra of MPDA, MPDA-TPP, DOX@MPDA-TPP, and DOX@MPDA-TPP@HA. Panel (J) refers to surface zeta potential measurements of MPDA-based nanoplatforms (MPDA, MPDA-TPP, DOX@MPDA-TPP, and DOX@MPDA-TPP@HA). Panel (K) is the hydrodynamic size of DOX@MPDA-TPP@HA over time in PBS and in serum-containing medium. Panel (L) is the hemolysis assay of DOX@MPDA-TPP@HA at various concentrations.

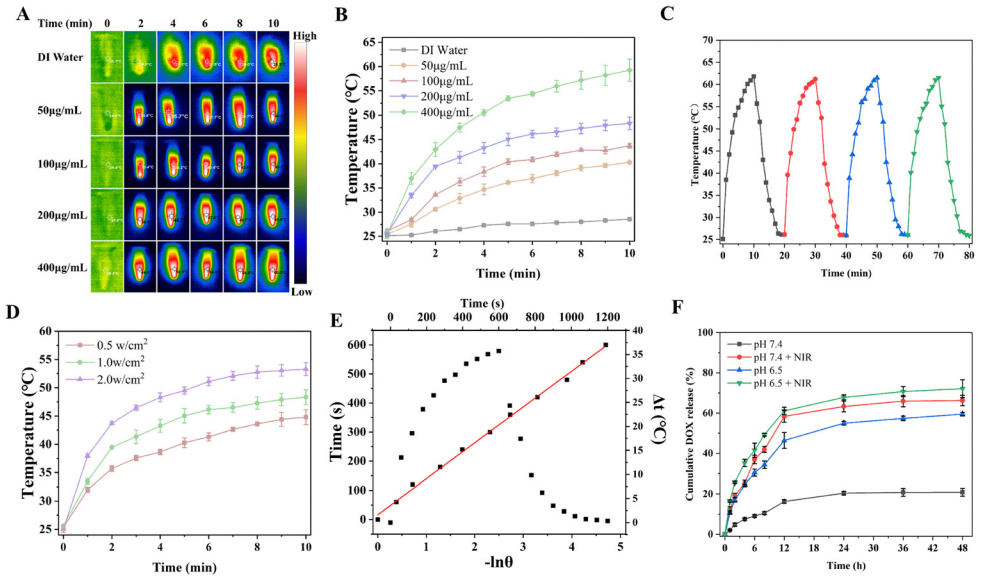

Fig. 2 Photothermal performance and pH/NIR-triggered drug release of DOX@MPDA-TPP@HA. (A) Infrared thermal images of DOX@MPDA-TPP@HA dispersions at varying concentrations under 808 nm laser irradiation (1.0 W cm^{-2}), recorded at 0, 2, 4, 6, 8, and 10 minutes. (B) Temperature elevation profiles of DOX@MPDA-TPP@HA at different concentrations under 808 nm laser (1.0 W cm^{-2}), corresponding to Panel (A). (C) Photothermal stability of DOX@MPDA-TPP@HA (400 μg mL^{-1}) over four cycles of laser on/off irradiation. (D) Laser power-dependent heating profiles of DOX@MPDA-TPP@HA (0.5, 1.0, and 2.0 W cm^{-2}; 808 nm). (E) Cooling curve and linear fitting of $-\ln(\theta)$ *versus* time for determining τ_s and photothermal conversion efficiency (η). (F) Cumulative DOX release in PBS at pH 7.4 and pH 6.5 with or without NIR irradiation (808 nm, 1.0 W cm^{-2}, 5 min).

illustrating both the loading capacity and photothermal competence of MPDA carriers.[9] Motivated by this versatility, the present work employs a doxorubicin-loaded, mitochondria-targeted, HA-coated MPDA platform (DOX@MPDA-TPP@HA) for HCC. The LC and EE of DOX@MPDA-TPP@HA were 14.6% and 51.3%, respectively, as calculated from the DOX calibration curve (Fig. S2). Under 808 nm irradiation at 1.0 W cm^{-2}, DOX@MPDA-TPP@HA dispersions exhibited time- and concentration-dependent heating over 10 min, whereas water showed negligible change (Fig. 2A and B). At 200 μg mL^{-1} the bulk temperature reached 48.3 °C, and four irradiation–cooling cycles at 400 μg mL^{-1} produced nearly overlapping peaks (Fig. 2C), indicating a stable photothermal response; at fixed concentration, higher power densities yielded larger temperature rises (Fig. 2D). Analysis of the heating and cooling traces gave τ_s = 158.4 s and $\eta \approx 30.5\%$ (Fig. 2E), consistent with PDA-based photothermal agents. Based on the power-dependent profiles, 1.0 W cm^{-2} was selected for subsequent release assays.

Release profiles highlight two orthogonal controls. First, at the same pH, brief NIR pulses at preset time points (808 nm, 1.0 W cm^{-2}, 5 min) markedly increased cumulative release at 48 h, from 20.8% to 66.2% at pH 7.4 and from 59.5% to 72.1% at pH 6.5 (Fig. 2F). This NIR effect is consistent with temperature-driven increases in doxorubicin diffusivity as viscosity decreases with temperature, together with thermal fluctuations that weaken noncovalent adsorption to the PDA framework and increase segmental mobility within the mesoporous matrix, thereby facilitating pore-to-bulk transport. Second, under the same irradiation state, release was greater at pH 6.5 than at pH 7.4, both without NIR (59.5% *versus* 20.8%) and with NIR pulses (72.1% *versus* 66.2%). The pH dependence can be rationalized by protonation of doxorubicin and of PDA catechol or amine sites at mildly acidic pH, which reduces net electrostatic attraction, perturbs π–π and hydrogen-bonding contributions through changes in electronic density and hydration, and increases doxorubicin solubility; these factors collectively lower the adsorption free energy and favor desorption from mesochannels.

Taken together, the cycling-stable photothermal behavior with $\eta \approx 30.5\%$ and the dual control by pH and NIR provide a coherent physical basis for coupling chemotherapy with photothermal heating in subsequent *in vitro* and *in vivo* evaluations.

3.2. Cellular uptake behavior of MPDA-based nanoplatforms

Efficient intracellular delivery is essential for nanoparticle-mediated chemotherapy. CD44, often overexpressed on tumor cells, binds HA and mediates endocytosis of HA-decorated nanoparticles, thereby enhancing delivery of therapeutics such as DOX. In CD44-positive Huh7 cells, uptake of DOX@MPDA-TPP and DOX@MPDA-TPP@HA was evaluated after 2 or 4 h. CLSM was performed under identical acquisition parameters, and intracellular DOX was quantified as mean fluorescence intensity (MFI) from ROI-defined fields. CLSM analysis (Fig. 3A and B) showed higher intracellular DOX fluorescence at 4 h than at 2 h for both MPDA-based nanoplatforms. At each time point, DOX@MPDA-TPP@HA produced stronger intracellular fluorescence than DOX@MPDA-TPP, whereas the untreated control displayed only baseline (autofluorescence) levels. Flow cytometry (Fig. 3C–E) was consistent with the microscopy findings. Relative to the untreated control, fluorescence

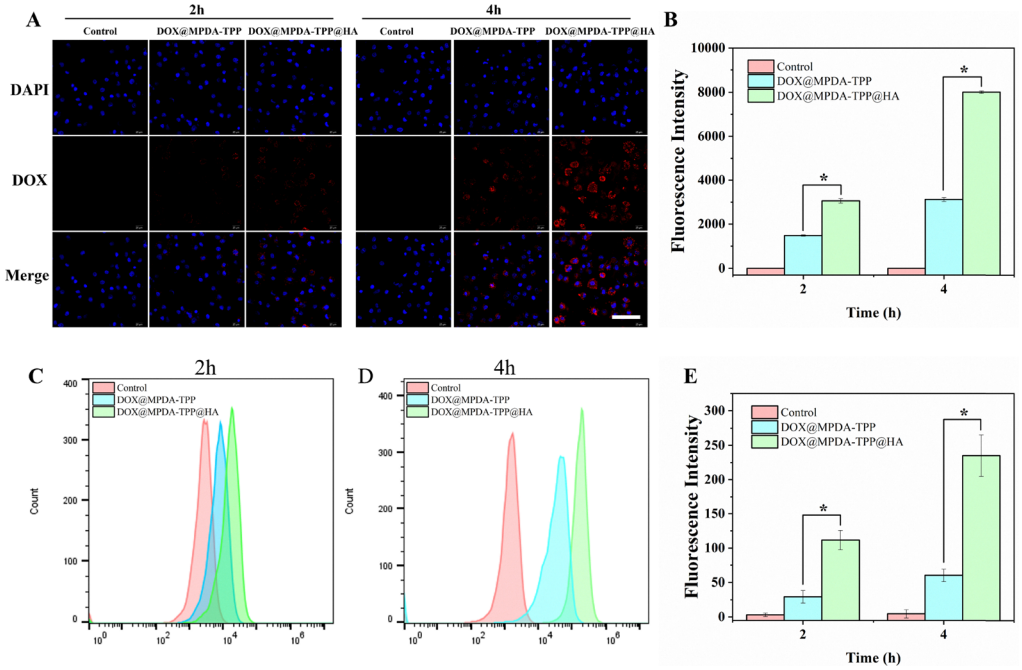

Fig. 3 Cellular uptake of DOX-loaded MPDA nanoplatforms in Huh7 cells. (A) CLSM images after 2 h and 4 h incubation for control, DOX@MPDA-TPP, and DOX@MPDA-TPP@HA. Scale bar: 100 μm. (B) Quantification of intracellular DOX fluorescence from CLSM images at 2 h and 4 h. (C) and (D) Flow-cytometry fluorescence histograms after 2 h (C) and 4 h (D) incubation for control, DOX@MPDA-TPP, and DOX@MPDA-TPP@HA. (E) Flow-cytometry quantification of cellular fluorescence at 2 h and 4 h. Data are mean ± SD (n = 3), * $p < 0.05$.

distributions for both nanoparticle treatments shifted toward higher intensities, and at 2 h and 4 h DOX@MPDA-TPP@HA yielded higher cellular fluorescence than DOX@MPDA-TPP. To assess the contribution of HA to uptake, a flow-cytometry comparison was performed (Fig. S3). Among all groups, DOX@MPDA-TPP@HA showed the highest cellular uptake. In the blocking condition, in which cells were preincubated with free HA before exposure to the nanocarriers, uptake of free HA + DOX@MPDA-TPP@HA decreased to approximately the DOX@MPDA-TPP level, whereas free HA + DOX@MPDA-TPP remained comparable to DOX@MPDA-TPP.

HA decoration enhances cellular uptake primarily through CD44 binding and receptor-mediated endocytosis. Multivalent HA on the nanoparticle surface increases effective avidity at the plasma membrane, promotes CD44 clustering, and facilitates internalization. HA coronas can also attenuate nonspecific protein adsorption and off-target phagocytic uptake, preserving ligand accessibility for CD44 engagement on tumor cells.[24] Under the present uptake conditions, DOX@MPDA-TPP@HA produced higher intracellular DOX fluorescence than DOX@MPDA-TPP, consistent with HA–CD44–mediated enhancement of internalization.

Mitochondria play a central role in intrinsic apoptosis and are closely linked to chemotherapy- and ROS-driven cell death.[25,26] In Fig. 4, Huh7 cells stained with MitoTracker Green (mitochondria) and DAPI (nuclei) show a stepwise increase in colocalization of the DOX signal (red) across the series from DOX@MPDA to DOX@MPDA-TPP to DOX@MPDA-TPP@HA. The corresponding Pearson correlation coefficients (PCC) are 0.49, 0.62, and 0.78, indicating stronger mitochondrial association after TPP conjugation and a further increase with HA coating (scale bar, 50 μm). The data are consistent with a mechanism in which TPP^+ mediates $\Delta\Psi_m$-dependent mitochondrial enrichment,[27,28] and HA increases overall uptake to further augment colocalization with mitochondria (Fig. 3).

3.3. *In vitro* antitumor efficacy of MPDA-based nanoplatforms

Fig. 5A evaluated biocompatibility by co-incubating L929 fibroblasts for 24 h with MPDA-based nanoplatforms at 25–400 μg mL^{-1}. Cell viability was above 90% at 25–200 μg mL^{-1} and remained above 85% at 400 μg mL^{-1}. These results indicate that MPDA-based nanoplatforms are well tolerated within this concentration range. For antitumor testing in Huh7 cells (Fig. 5B), treatments were applied at 6.25–100 μg mL^{-1}. NIR irradiation was delivered to the designated groups to the designated groups at 808 nm, 1.0 W cm^{-2} for 5 min. The largest reduction in cell viability occurred with DOX@MPDA-TPP@HA + NIR, followed by MPDA-TPP@HA + NIR. Without NIR irradiation, DOX@MPDA-TPP@HA reduced viability more than free DOX at matched DOX doses; at 100 μg mL^{-1} the values were approximately 44.5% *versus* 54.9%. With irradiation, DOX@MPDA-TPP@HA + NIR decreased viability to about 20.5% (n = 3, *$P < 0.05$).

The live/dead assay (Fig. 5C and D) was consistent with the CCK-8 results in Fig. 5B, revealing clear differences in cell viability across treatment groups. In this assay, Calcein AM labels viable cells green, whereas propidium iodide marks dead cells in red. Control and MPDA-TPP@HA fields were dominated by green fluorescence with only sparse PI signal. With NIR

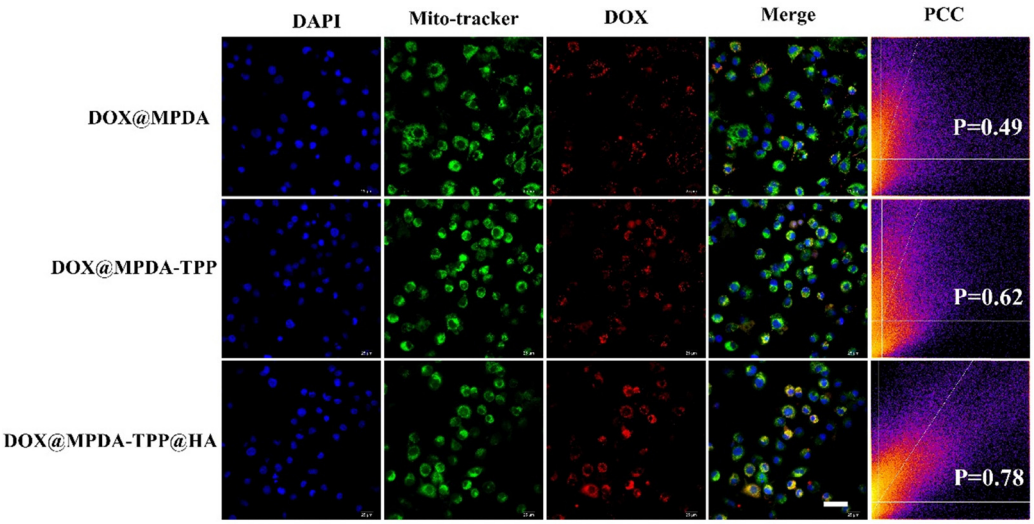

Fig. 4 Mitochondrial colocalization in Huh7 cells. CLSM images showing nuclei (DAPI, blue), mitochondria (MitoTracker Green), and DOX signal (red) after incubation with DOX@MPDA, DOX@MPDA-TPP, or DOX@MPDA-TPP@HA. Pearson's correlation coefficients (PCC) for DOX/mitochondria colocalization are indicated for each panel. Scale bar, 50 μm.

treatment (MPDA-TPP@HA + NIR), the proportion of PI-positive cells increased. Free DOX produced a higher PI-positive fraction than control and MPDA-TPP@HA, but a lower fraction than DOX@MPDA-TPP@HA and DOX@MPDA-TPP@HA + NIR. At matched DOX doses, DOX@MPDA-TPP@HA further increased nonviable cells, and DOX@MPDA-TPP@HA + NIR exhibited the largest PI-positive fraction. Quantification (Fig. 5D) confirmed this ordering with statistical significance ($^{*}P < 0.05$, $n = 3$).

Annexin V-FITC/PI flow cytometry (Fig. 5E and F) showed a similar pattern. Compared with control, MPDA-TPP@HA + NIR increased the proportions of early (Annexin V positive/PI negative) and late (Annexin V positive/PI positive) apoptosis. Free DOX further elevated apoptosis. At matched DOX dose, DOX@MPDA-TPP@HA produced a higher apoptotic fraction than free DOX, and DOX@MPDA-TPP@HA + NIR yielded the largest apoptotic fraction among all groups. Quantification in Fig. 5F confirmed this order: the apoptotic fraction was highest with DOX@MPDA-TPP@HA + NIR, followed by DOX@MPDA-TPP@HA, then DOX, then MPDA-TPP@HA + NIR, while MPDA-TPP@HA and control were lowest ($^{*}P < 0.05$, $n = 3$).

Overall, DOX@MPDA-TPP@HA with NIR produced the strongest cytotoxicity, attributable to hyaluronic-acid–mediated cellular delivery, triphenylphosphonium-driven mitochondrial localization, and near-infrared–facilitated doxorubicin availability. Hyaluronic acid increases CD44-mediated uptake, raising intracellular doxorubicin relative to free drug and to non-HA particles (Fig. 3). Triphenylphosphonium promotes mitochondrial association, positioning the payload at a central hub of apoptotic signaling and amplifying damage once chemothermal stress is applied (Fig. 4). The MPDA core efficiently converts 808 nm light to heat and, together with mildly acidic intracellular conditions, accelerates doxorubicin desorption from the polydopamine matrix, as indicated by concentration- and power-dependent heating, cycling stability, and pH/NIR-triggered release profiles (Fig. 2A–F). Taken together, the findings indicate that DOX@MPDA-TPP@HA with NIR shows the strongest cytotoxicity among all groups tested.

3.4. Effects of MPDA-based nanoplatforms on ROS and mitochondrial membrane potential in Huh7 cells

Mitochondria are a principal intracellular source of reactive oxygen species (ROS).[29] During PTT, local hyperthermia can disrupt the inner mitochondrial membrane and lower the membrane potential ($\Delta\Psi_m$). These injuries impair the electron transport chain, increase electron leakage to oxygen, and generate superoxide, which is subsequently converted to hydrogen peroxide and other ROS.[30,31] To evaluate ROS generation with the MPDA-based nanoplatforms, intracellular ROS in Huh7 cells was quantified using the DCFH-DA probe. Upon cellular uptake, DCFH-DA is de-esterified to non-fluorescent DCFH, which is oxidized by ROS to fluorescent DCF; the green fluorescence thus reflects the total intracellular ROS level. In Fig. 6A, control and MPDA-TPP@HA show faint green fluorescence. With NIR irradiation, MPDA-TPP@HA + NIR displays a higher signal. Free DOX yields a stronger signal than these groups, DOX@MPDA-TPP@HA is higher than free DOX, and the DOX@MPDA-TPP@HA + NIR group exhibits the highest fluorescence. Quantification in Fig. 6B confirmed this ordering, with DOX@MPDA-TPP@HA + NIR exceeding all other groups, indicating that combining chemotherapy and photothermal treatment elevates intracellular ROS relative to single-modality conditions.

Consistent with the confocal results (Fig. 6A and B), flow-cytometric analysis of DCF fluorescence showed condition-dependent increases in intracellular ROS (Fig. 6C and D). Under identical acquisition and gating parameters, the ROS signal was lowest in the control and MPDA-TPP@HA groups, increased with MPDA-TPP@HA + NIR, rose further with free

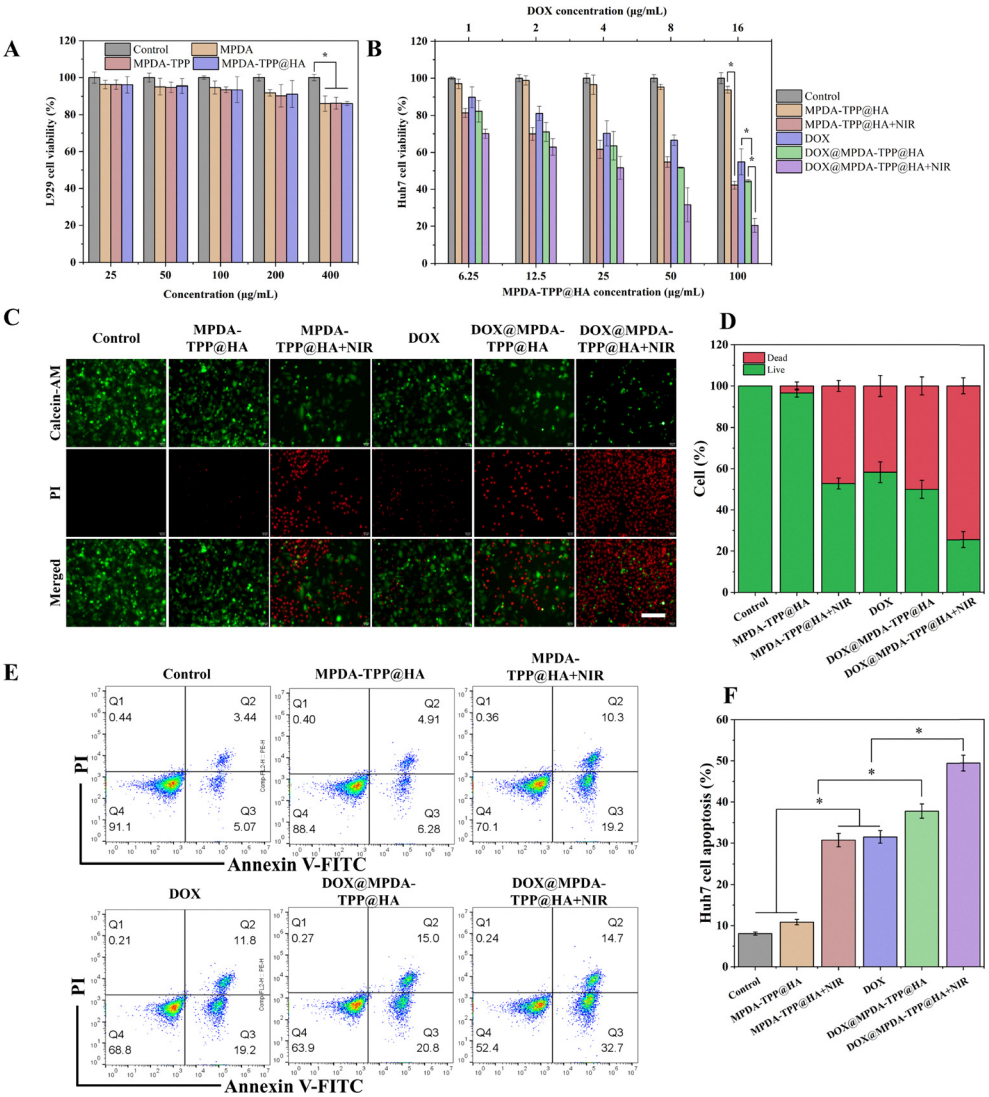

Fig. 5 *In vitro* cytotoxicity and apoptosis of MPDA-based nanoplatforms. (A) L929 cell viability after 24 h incubation with MPDA, MPDA-TPP, or MPDA-TPP@HA (25–400 μg mL^{-1}). (B) Huh7 cell viability after 24 h treatment with control, MPDA-TPP@HA, MPDA-TPP@HA + NIR, DOX, DOX@MPDA-TPP@HA, or DOX@MPDA-TPP@HA + NIR (6.25–100 μg mL^{-1}; top axis shows DOX equivalents 1–16 μg mL^{-1}). At each dose, DOX content was matched across the DOX, DOX@MPDA-TPP@HA, and DOX@MPDA-TPP@HA + NIR groups. (C) Live/dead fluorescence images for MPDA-based treatment groups (green = viable, red = non-viable). Scale bar, 200 μm. (D) Quantification of live and dead fractions corresponding to panel (C). (E) Flow-cytometry plots for apoptosis analysis of MPDA-based treatment groups. (F) Quantification of apoptosis corresponding to panel (E). Panels (C)–(F) include the following six groups: control, MPDA-TPP@HA, MPDA-TPP@HA + NIR, DOX, DOX@MPDA-TPP@HA, and DOX@MPDA-TPP@HA + NIR. NIR irradiation was applied to designated groups (808 nm, 1.0 W cm^{-2}, 5 min) at 8 h post-treatment. Data are mean ± SD (n = 3), * $p < 0.05$.

DOX, was greater with DOX@MPDA-TPP@HA, and was highest with DOX@MPDA-TPP@HA + NIR.

JC-1 was used to assess $\Delta\Psi_m$ in Huh7 cells. At high $\Delta\Psi_m$, JC-1 forms red fluorescent J-aggregates; upon depolarization it remains as green fluorescent monomers. Thus, a red-to-green shift indicates mitochondrial depolarization. In Fig. 6E, control and MPDA-TPP@HA show predominantly red signal with weak green, consistent with intact $\Delta\Psi_m$. MPDA-TPP@HA + NIR exhibits an obvious increase in green fluorescence, indicating partial depolarization. Free DOX further enhances the green component. DOX@MPDA-TPP@HA shows a more pronounced loss of red with increased green, and DOX@MPDA-TPP@HA + NIR displays the strongest red-to-green shift. Quantification in panel (F) (red/green fluorescence ratio) confirmed these findings: the ratio is highest in control and MPDA-TPP@HA, decreases with MPDA-TPP@HA + NIR, declines further with free DOX, is lower with DOX@MPDA-TPP@HA, and is lowest with DOX@MPDA-TPP@HA + NIR.

A plausible mechanism accounts for these trends. Dox undergoes quinone/semiquinone redox cycling and perturbs mitochondrial respiration, thereby increasing ROS formation.[32] The TPP^+ moiety drives mitochondrial enrichment of the nanoplatform, raising the local drug concentration within mitochondria.[27,28] Upon 808 nm irradiation, the MPDA core generates localized hyperthermia at mitochondria. The resulting thermal stress perturbs the inner-mitochondrial membrane

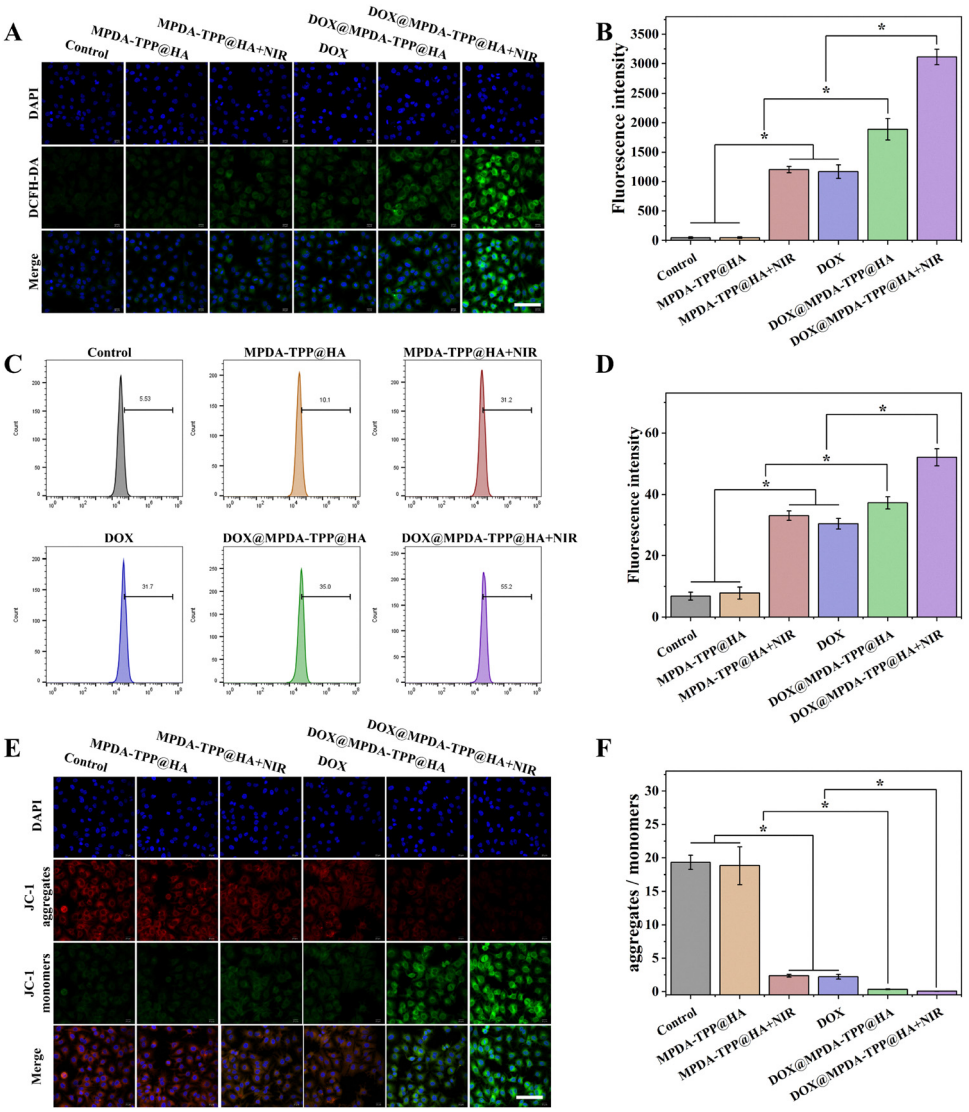

Fig. 6 Intracellular ROS and mitochondrial membrane potential in Huh7 cells. Huh7 cells were treated for 24 h with one of the following groups: control, MPDA-TPP@HA, MPDA-TPP@HA + NIR, DOX, DOX@MPDA-TPP@HA, DOX@MPDA-TPP@HA + NIR. NIR irradiation was applied to designated groups (808 nm, 1.0 W cm^{-2}, 5 min) at 8 h post-treatment. (A) Confocal images of DCFH-DA fluorescence (ROS, green) with DAPI nuclei (blue). Scale bar: 100 μm. (B) Quantification of intracellular ROS from panel (A). (C) Flow-cytometry histograms of DCF fluorescence. (D) Flow-cytometric quantification of intracellular ROS. (E) JC-1 staining for $\Delta\Psi_m$: red J-aggregates indicate polarized mitochondria; green monomers indicate depolarization. Scale bar, 100 μm. (F) Red/green fluorescence ratio calculated from panel (E). Data are mean ± SD (n = 3), * $p < 0.05$.

and impairs electron-transport chain function (complexes I and III), leading to $\Delta\Psi_m$ dissipation and increased proton leak. These changes prolong the lifetime of reduced intermediates and increase electron leakage to molecular oxygen, thereby amplifying mitochondrial ROS production. Taken together, these effects account for the maximal ROS signal observed in the DOX@MPDA-TPP@HA + NIR group.

3.5. Immunogenic cell death induced by MPDA-based nanoplatforms

ICD proceeds through coordinated danger-associated molecular patterns (DAMPs), including CRT exposure on the plasma membrane and nuclear release of HMGB1. In Huh7 cells, membrane CRT was visualized by immunofluorescence under identical acquisition settings (Fig. 7A) and quantified as mean fluorescence intensity (Fig. 7B). Signals were minimal in the control and MPDA-TPP@HA. NIR irradiation of MPDA-TPP@HA increased CRT exposure. Free DOX induced stronger CRT than these groups. DOX@MPDA-TPP@HA further enhanced CRT, and the maximal level occurred with DOX@MPDA-TPP@HA + NIR.

HMGB1 localization exhibited a complementary pattern to CRT exposure, reflecting another key hallmark of ICD. Under identical acquisition settings, HMGB1 fluorescence was predominantly confined to the nucleus in both the control group and the MPDA-TPP@HA group, indicating negligible baseline translocation and minimal spontaneous ICD activity (Fig. 7C). Upon NIR irradiation of MPDA-TPP@HA, nuclear HMGB1 levels began to decrease, suggesting partial

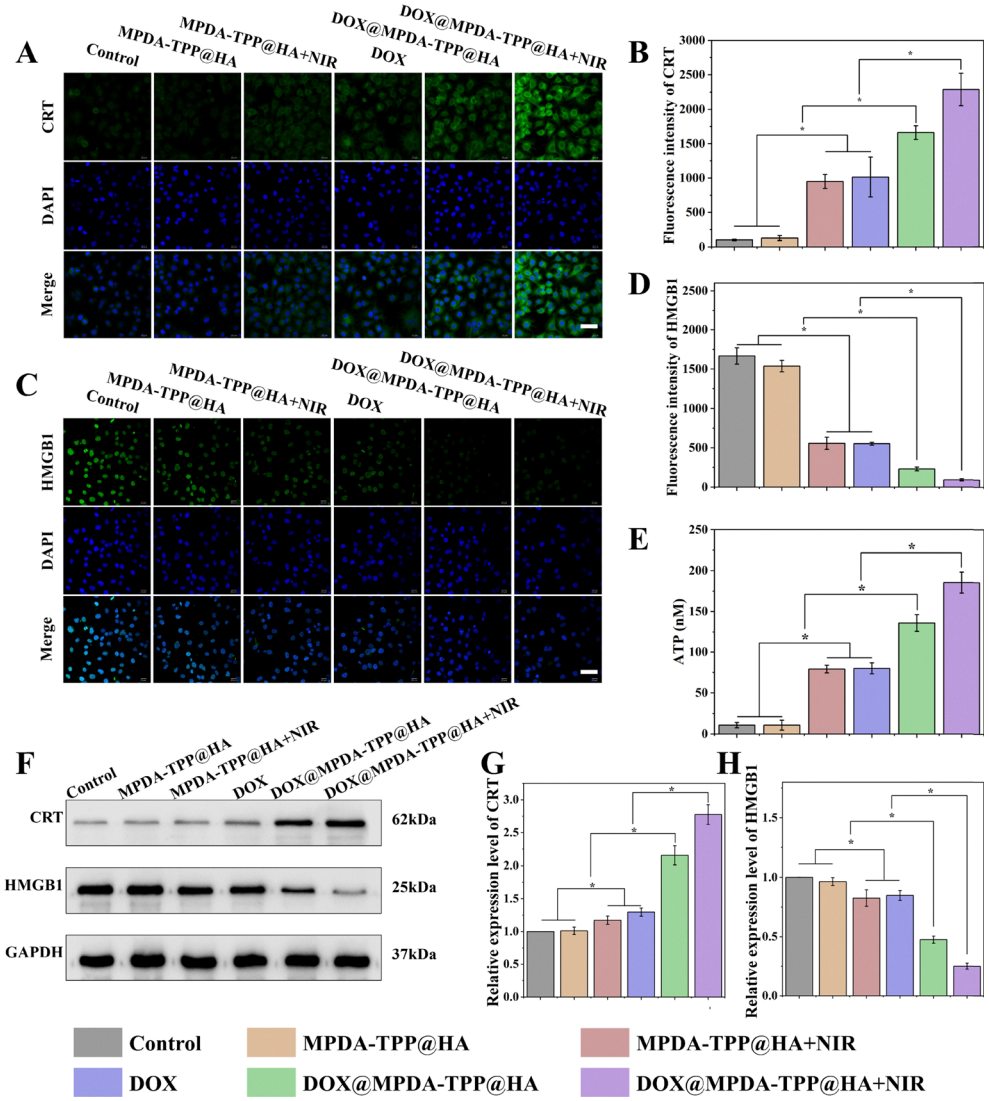

Fig. 7 Evaluation of ICD markers in Huh7 cells following various treatments. Huh7 cells were treated for 24 h with one of the following groups: control, MPDA-TPP@HA, MPDA-TPP@HA + NIR, DOX, DOX@MPDA-TPP@HA, DOX@MPDA-TPP@HA + NIR. NIR irradiation was applied to designated groups (808 nm, 1.0 W cm^{-2}, 5 min) at 8 h post-treatment. (A) CLSM images of CRT exposure on the plasma membrane. (B) Quantitative analysis of CRT fluorescence intensity. (C) CLSM images showing HMGB1 localization in the nucleus and cytoplasm. (D) Quantification of nuclear HMGB1 intensity. (E) ATP levels cell culture supernatant determined by luminescence assay. (F) western blot analysis of CRT and HMGB1 protein expression in cell lysates. (G) and (H) Quantitative analysis of CRT and HMGB1 protein expression from western blots, based on band intensity and normalized to GAPDH. Data are mean ± SD (n = 3), * $p < 0.05$.

photothermal-induced stress. Free DOX further reduced nuclear HMGB1, consistent with its capacity to initiate ICD. DOX@MPDA-TPP@HA induced a more pronounced decrease in nuclear HMGB1 at an equivalent drug dose, reflecting the additive effect of nanoparticle-mediated delivery. The most substantial nuclear depletion was observed in the DOX@MPDA-TPP@HA + NIR group, indicating robust HMGB1 translocation to the cytoplasm and/or extracellular milieu. Quantitative analysis of nuclear fluorescence intensity (Fig. 7D) confirmed these trends. These results are consistent with the elevated intracellular ROS and mitochondrial depolarization observed in Fig. 6, both of which are potent upstream triggers of HMGB1 release.

Another hallmark of ICD is ATP release into the extracellular space, which functions as a potent 'find-me' signal for dendritic cells. To assess this feature, we quantified extracellular ATP from Huh7 cells under different treatments using a luminescence-based ATP assay (Fig. 7E). Minimal ATP release was detected in the control and MPDA-TPP@HA groups, suggesting low basal immunogenicity. Upon NIR irradiation, MPDA-TPP@HA + NIR induced a modest increase in ATP, consistent with its mild photothermal stress. Free DOX led to a more pronounced release, while DOX@MPDA-TPP@HA triggered greater ATP release at the same DOX dose. The combination of DOX@MPDA-TPP@HA + NIR resulted in the highest extracellular ATP levels, indicating enhanced ICD activation when chemotherapy and photothermal therapy were combined.

To validate these findings, western blotting of CRT and HMGB1 was performed with GAPDH as the loading control

(Fig. 7F), followed by densitometry normalized to GAPDH (Fig. 7G and H). CRT levels increased from DOX to DOX@MPDA-TPP@HA and were maximal with DOX@MPDA-TPP@HA + NIR (Fig. 7G). Intracellular HMGB1 showed the opposite trend and was lowest with DOX@MPDA-TPP@HA + NIR (Fig. 7H). Together, these data indicate that combining chemotherapy with photothermal treatment induces the strongest ICD signature in Huh7 cells.

3.6. *In vivo* antitumor efficacy of MPDA-based nanoplatforms

To evaluate the tumor-targeting capability of DOX@MPDA-TPP@HA nanoparticles *in vivo*, a small animal live imaging system was used to monitor the biodistribution in Huh7 tumor-bearing mice. As shown in Fig. 8A and B, fluorescence intensity at the tumor site was higher in the DOX@MPDA-TPP@HA group than in the DOX@MPDA-TPP group throughout the observation period, suggesting enhanced tumor accumulation. This improvement is likely due to the HA modification, which prolongs circulation time and promotes CD44 receptor-mediated tumor targeting. The fluorescence signal at the tumor site peaked at 12 hours post-injection, indicating an optimal time window for therapeutic intervention. To assess biodistribution in major organs, *ex vivo* imaging was performed at 24 hours post-injection (Fig. 8C). Quantitative analysis showed higher fluorescence intensity in tumors from the DOX@MPDA-TPP@HA group compared to the non-HA-modified group, further confirming improved tumor localization. Meanwhile, fluorescence signals in non-tumor organs (heart, liver, spleen, lung, and kidney) were relatively low, reflecting reduced off-target accumulation and favorable tumor-to-organ distribution.

To investigate photothermal performance, tumor-bearing mice were injected with nanoparticles, and 12 hours later, tumors were irradiated with an 808 nm NIR laser. As shown in Fig. 8D and E, the tumor temperature in the DOX@MPDA-TPP@HA group rapidly increased from 34.5 °C to 50.3 °C, which was higher than the 42.3 °C recorded in the DOX@MPDA-TPP group. The control group showed minimal temperature change, indicating the absence of a photothermal effect. These results demonstrate that HA-functionalized nanoplatform enable efficient *in vivo* photothermal conversion and targeted heat generation, which is essential for localized tumor ablation.

To assess *in vivo* therapeutic efficacy, Huh7 tumor-bearing mice were treated as shown in Fig. 8F. Tumor volume tracking

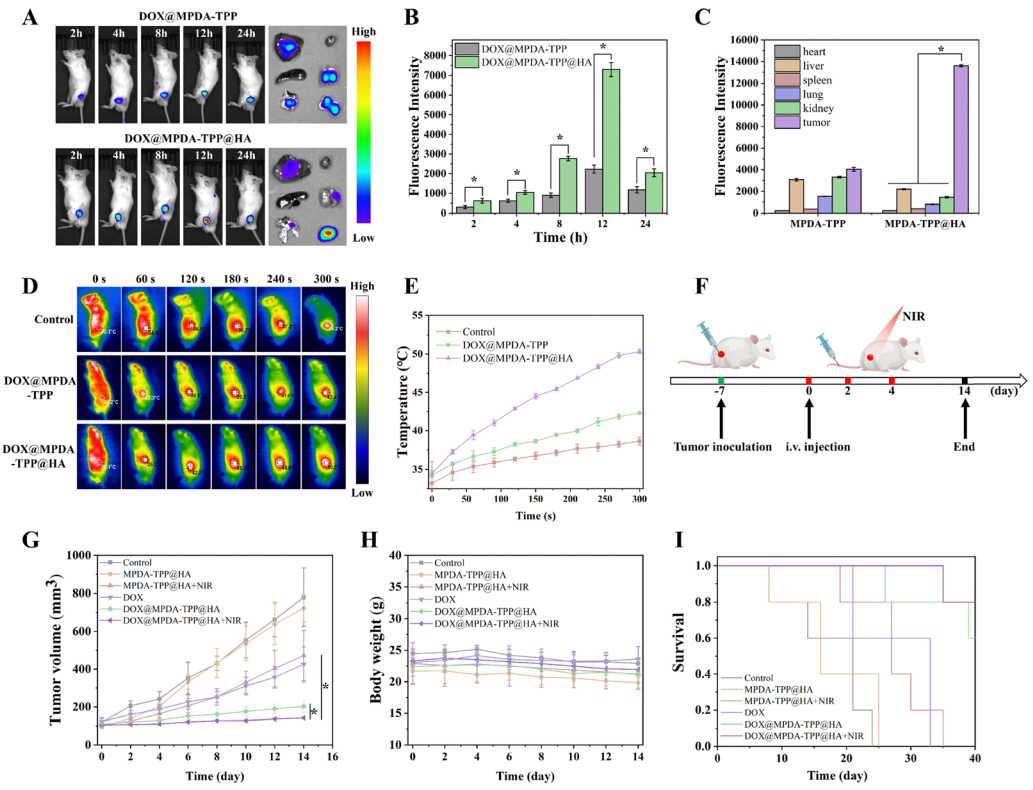

Fig. 8 *In vivo* biodistribution, photothermal effect, and antitumor efficacy of DOX@MPDA-TPP@HA nanoplatform in Huh7 tumor-bearing mice. (A) Representative fluorescence images showing the biodistribution of DOX@MPDA-TPP and DOX@MPDA-TPP@HA at different time points after intravenous injection. (B) Quantitative analysis of fluorescence intensity at the tumor site over time. (C) *Ex vivo* fluorescence intensity in major organs and tumors 24 h post-injection. (D) Infrared thermal imaging of tumor-bearing mice during 300 s NIR laser irradiation (808 nm, 1.0 W cm^{-2}) after different treatments. (E) Tumor site temperature variation recorded every 20 s during laser exposure. (F) Schematic illustration of the treatment timeline: tumor inoculation (day 7), nanoplatform injection (day 0), NIR irradiation (day 2 and day 4), and study endpoint (day 14). (G) Tumor volume changes in different treatment groups. (H) Body weight monitoring throughout the treatment period to evaluate systemic toxicity. (I) Survival curves of mice under different treatment conditions.

(Fig. 8G) showed that the control and MPDA-TPP@HA groups did not suppress tumor growth, indicating that the carrier alone lacks therapeutic activity. Tumor inhibition was observed in the MPDA-TPP@HA + NIR, DOX, DOX@MPDA-TPP@HA, and DOX@MPDA-TPP@HA + NIR groups. Among these, DOX@MPDA-TPP@HA reduced tumor volume compared with free DOX, likely due to improved tumor targeting and drug delivery. The greatest reduction in tumor volume was observed in the DOX@MPDA-TPP@HA + NIR group, suggesting a synergistic interaction between chemotherapy and PTT. Body weight remained stable across all groups during the treatment period (Fig. 8H), supporting good systemic tolerability of the nanoplatforms. Furthermore, survival analysis (Fig. 8I) indicated that the DOX@MPDA-TPP@HA + NIR group exhibited the highest survival rate, further highlighting the potential advantage of combination therapy.

To further evaluate the effects of the nanoparticles on tumor cells, tumors were excised (Fig. 9A) and subjected to histological and immunofluorescence analysis to assess cell proliferation, apoptosis, and ROS levels. As shown in Fig. 9B, tumors in the DOX@MPDA-TPP@HA + NIR group exhibited the most extensive cellular deformation, nuclear condensation, and necrotic regions on H&E staining compared with other groups. Ki67 staining, which reflects cellular proliferation, revealed strong positive signals in the control and MPDA-TPP@HA groups, while reduced Ki67 expression was observed in the MPDA-TPP@HA + NIR, DOX, DOX@MPDA-TPP@HA, and DOX@MPDA-TPP@HA + NIR groups (Fig. 9C). TUNEL staining showed the highest apoptotic signal in the DOX@MPDA-TPP@HA + NIR group, with an apoptosis rate of 45.6% (Fig. 9D). Intratumoral ROS levels were evaluated using DCFH-DA staining. The DOX@MPDA-TPP@HA + NIR group showed the highest fluorescence intensity among all groups (Fig. 9E), indicating enhanced ROS generation.

3.7. *In vivo* antitumor immune response induced by MPDA-based nanoplatforms

To evaluate whether DOX@MPDA-TPP@HA combined with photothermal therapy (PTT) enhances ICD and stimulates a stronger *in vivo* immune response, we performed immunofluorescence staining of tumor sections to detect the expression of CRT, HMGB1, $CD8^+$ T cells, and $CD4^+$ T cells across different treatment groups. As shown in Fig. 10A, the DOX@MPDA-TPP@HA + NIR group exhibited the most intense red fluorescence for CRT, with expression levels 5.9-, 5.8-, 2.3-, 2.3-, and 1.4-fold higher than those in the control, MPDA-TPP@HA, MPDA-TPP@HA + NIR, DOX, and DOX@MPDA-TPP@HA groups, respectively (Fig. 10B). Moreover, green fluorescence

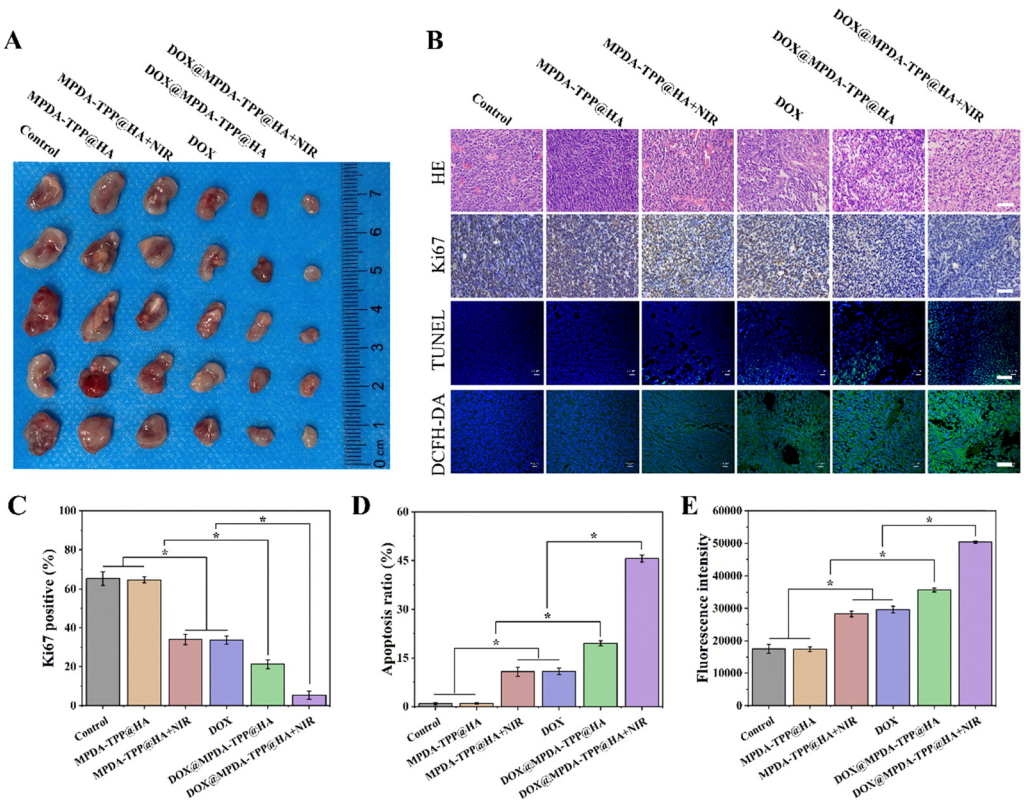

Fig. 9 Histological and immunofluorescence evaluation of therapeutic effects in tumor tissues after different treatments. (A) Representative images of excised tumors from each treatment group. (B) H&E and immunofluorescence staining of tumor sections for Ki67, TUNEL, and DCFH-DA (ROS levels). Scale bars: 60 μm. (C) Quantification of Ki67-positive cells to assess tumor cell proliferation across treatment groups. (D) Quantification of apoptotic cells based on TUNEL staining. (E) Quantification of ROS levels in tumor tissues measured by DCFH-DA fluorescence intensity. Data are mean ± SD (n = 3), * $p < 0.05$.

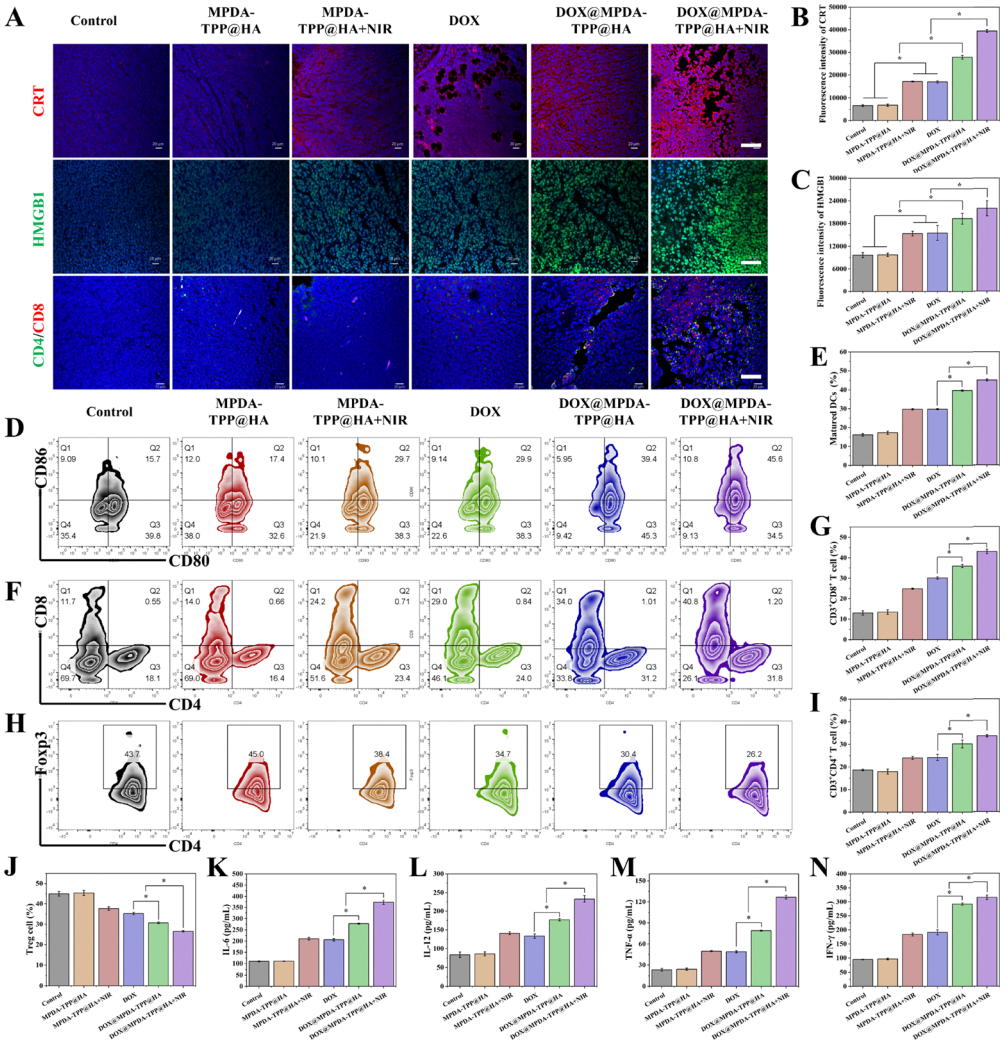

Fig. 10 *In vivo* ICD induction and immune response activation by DOX@MPDA-TPP@HA combined with NIR irradiation. (A) Immunofluorescence staining of tumor tissues from mice treated with different treatment groups using anti-CRT, anti-HMGB1, anti-CD4, and anti-CD8 antibodies. Scale bar: 60 μm. (B) and (C) Quantification of CRT and HMGB1 fluorescence intensity, respectively. (D) and (E) Flow cytometric analysis and quantification of mature dendritic cells ($CD11c^+CD80^+CD86^+$) in tumor-draining lymph nodes following different treatments. (F) Flow cytometry analysis of intratumoral $CD4^+$ and $CD8^+$ T cells (gated on $CD3^+$ T cells). (G) and (H) Quantification of $CD3^+CD8^+$ and $CD3^+CD4^+$ T cells in tumor tissues. (I) and (J) Flow cytometry analysis and quantification of regulatory T cells (Tregs, $CD3^+CD4^+Foxp3^+$) within tumors. (K)–(N) Cytokine levels of IL-6, IL-12, TNF-α, and IFN-γ in tumor homogenates. Data are mean ± SD (n = 3), * $p < 0.05$.

corresponding to HMGB1 was substantially enhanced in the MPDA-TPP@HA + NIR, DOX, DOX@MPDA-TPP@HA, and DOX@MPDA-TPP@HA + NIR groups (Fig. 10A and C), indicating increased release and translocation of HMGB1 from the nucleus to the cytoplasm—a hallmark of ICD. Collectively, these findings demonstrate that DOX@MPDA-TPP@HA nanoplatform, when combined with PTT, effectively promote ICD in tumor tissues and potentially initiate a robust antitumor immune response.

Dendritic cells (DCs) are typically found in an immature state; however, upon exposure to appropriate stimuli, they undergo maturation and migrate to lymphoid organs and tumor sites. This maturation is essential for activating cytotoxic T lymphocytes (CTLs), which play a central role in antitumor immunity. To evaluate immune activation, we assessed the maturation status of DCs in TDLNs using flow cytometry. CD11c serves as a key DC marker, while CD80 and CD86 are critical costimulatory molecules involved in T cell activation *via* interaction with CD28. The proportions of $CD80^+$ and $CD86^+$ DCs were used as indicators of maturation. As shown in Fig. 10D and E, the percentage of mature DCs in the control and MPDA-TPP@HA groups was 16.1% and 17.2%, respectively. Higher maturation rates were observed in the MPDA-TPP@HA + NIR, DOX, and DOX@MPDA-TPP@HA groups (29.7%, 29.8%, and 39.7%, respectively). Notably, the DOX@MPDA-TPP@HA + NIR group showed the highest maturation rate at 45.1%, approximately 2.8 times higher than the control. During maturation, DCs enhance their capacity to process and present antigens, initiating robust antigen-specific T cell responses. To further evaluate this immune activation, we analyzed T cell infiltration within the tumor microenvironment (TME). CD3

identifies total T lymphocytes, with $CD3^+CD8^+$ and $CD3^+CD4^+$ cells corresponding to CTLs and helper T cells, respectively.

Flow cytometry revealed varied levels of T cell infiltration among treatment groups. As shown in Fig. 10F, the DOX@MPDA-TPP@HA + NIR group exhibited the highest infiltration levels, with $CD3^+CD4^+$ and $CD3^+CD8^+$ T cells increasing by 1.8-fold and 3.3-fold, respectively, compared to the control (Fig. 10G and I).

In addition, regulatory T cells (Tregs) play a pivotal role in facilitating tumor immune evasion and supporting tumor cell survival. Tumor cells can secrete signaling molecules that actively recruit Tregs into the tumor microenvironment (TME), thereby inducing immunosuppression or immune tolerance and ultimately exacerbating tumor immune escape. As such, the abundance of Tregs serves as a key indicator for evaluating the immunosuppressive state of the tumor. Tregs are typically characterized by the co-expression of CD4 and CD25 surface markers and high levels of the transcription factor Foxp3. To evaluate whether nanoparticle treatment effectively suppressed Treg accumulation, we analyzed the proportion of $CD3^+CD4^+Foxp3^+$ T cells in tumor tissues. As shown in Fig. 10H and J, the proportion of Tregs in the control group was 45.0%. In contrast, treatment with MPDA-based therapeutic nanoplatform reduced Treg levels. The DOX@MPDA-TPP@HA + NIR group exhibited a marked reduction in Treg frequency to 26.6%. These results suggest that combining DOX@MPDA-TPP@HA nanoparticles with PTT can effectively attenuate Treg-mediated immunosuppression within the TME and enhance antitumor immune responses.

Furthermore, the initiation of effective antitumor immunity is often accompanied by increased secretion of pro-inflammatory cytokines such as IL-6, IL-12, TNF-α, and IFN-γ. To assess the cytokine profile within tumor tissues, ELISA assays were performed. As shown in Fig. 10K–N, the levels of all four cytokines increased to varying degrees following nanoparticle administration, with the DOX@MPDA-TPP@HA + NIR group demonstrating the highest concentrations across all markers.

To evaluate the *in vivo* biosafety of DOX@MPDA-TPP@HA, healthy mice were intravenously injected with the nanoplatforms, followed by assessments of hematological, biochemical, and histopathological parameters over a 14-day period (Fig. S4). Routine blood tests showed that white blood cell (WBC), red blood cell (RBC), and platelet (PLT) counts remained within normal ranges and did not show apparent deviations compared to the untreated control group (Fig. S4A–C). Serum biochemical markers used to evaluate cardiac, renal, and hepatic function, including creatine kinase (CK), creatinine (CRE), and alanine aminotransferase (ALT), also remained stable and comparable to control values (Fig. S4D–F).

Histological examination of major organs, including the heart, liver, spleen, lungs, and kidneys, was performed on day 14. Hematoxylin and eosin (H&E) staining revealed no signs of tissue damage, necrosis, or inflammatory cell infiltration (Fig. S4G). These findings suggest that DOX@MPDA-TPP@HA has excellent biocompatibility and does not cause acute systemic toxicity *in vivo*. The targeted and controlled release of the drug from the nanoparticle system reduces the adverse effects typically associated with free DOX while maintaining antitumor efficacy. This favorable safety profile supports its potential for clinical translation, particularly in tumor treatments requiring long-term or repeated administration.

4. Conclusion

In summary, we have successfully developed a mitochondria-targeted and hyaluronic acid-modified mesoporous polydopamine nanoplatform (DOX@MPDA-TPP@HA) for combined chemo–photothermal therapy and immune modulation. The nanoplatform exhibited strong photothermal conversion efficiency, pH/thermal-responsive drug release behavior, and precise mitochondrial localization due to TPP modification. Furthermore, enhanced tumor targeting was achieved *via* HA–CD44 interaction, enabling effective induction of ICD, promotion of dendritic cell maturation, and increased intratumoral infiltration of $CD8^+$ and $CD4^+$ T cells. Importantly, the treatment strategy also reduced Treg accumulation and alleviated the immunosuppressive tumor microenvironment. Collectively, this multifunctional nanoplatform represents a promising approach for synergistic cancer therapy by integrating photothermal, chemotherapeutic, and immune-stimulating effects.

Author contributions

Haizhou Qiu, conceptualization, methodology, investigation, data analysis, and original draft writing; Kunlin Chen, material synthesis, *in vitro* experiments, and data curation; Yiwen Qiu, experimental design refinement, mechanism exploration, and data interpretation; Yi Yang, data acquisition; Tao Wang, data collection; Li Jiang, project supervision, resource coordination, and manuscript review; Wentao Wang, principal supervision, conceptual guidance, and final manuscript revision.

Conflicts of interest

The authors declare that there is no potential conflict of interest and no commercial or financial relationships in this study.

Data availability

The data supporting this article have been included as part of the supplementary information (SI). Supplementary information is available. See DOI: **https://doi.org/10.1039/d5tb01901j**.

Acknowledgements

This study was supported by the National Natural Science Foundation of China (82470652, 82170543), the Sichuan

Natural Science Foundation Project (24NSFSC0237), as well as the Science and Technology Program of the Sichuan Science and Technology Department (2025ZNSFSC1684).

References

1 Q. Li, C. Ding, M. Cao, F. Yang, X. Yan and S. He, *et al.*, Global epidemiology of liver cancer 2022: An emphasis on geographic disparities, *Chin. Med. J.*, 2024, **137**(19), 2334–2342.
2 A. Sarveazad, S. Agah, A. Babahajian, N. Amini and M. Bahardoust, Predictors of 5 year survival rate in hepatocellular carcinoma patients, *J. Res. Med. Sci.*, 2019, **24**, 86.
3 S. Daher, M. Massarwa, A. A. Benson and T. Khoury, Current and Future Treatment of Hepatocellular Carcinoma: An Updated Comprehensive Review, *J. Clin. Transl. Hepatol.*, 2018, **6**(1), 69–78.
4 Y. Zou, X. Wan, Q. Zhou, G. Zhu, S. Lin and Q. Tang, *et al.*, Mechanisms of drug resistance in hepatocellular carcinoma, *Biol. Proced. Online*, 2025, **27**(1), 19.
5 Z. Sas, E. Cendrowicz, I. Weinhäuser and T. P. Rygiel, Tumor Microenvironment of Hepatocellular Carcinoma: Challenges and Opportunities for New Treatment Options, *Int. J. Mol. Sci.*, 2022, **23**(7), 3778.
6 Y. Liu, C. Wang, S. Liu, H. Ma, J. Xu and K. Jiang, *et al.*, Mesoporous Polydopamine Nanotherapeutics for MRI-Guided Cancer Photothermal and Anti-Inflammatory Therapy, *Int. J. Nanomed.*, 2024, **19**, 10819–10837.
7 R. Chen, B. Lin and R. Luo, Recent progress in polydopamine-based composites for the adsorption and degradation of industrial wastewater treatment, *Heliyon*, 2022, **8**(12), e12105.
8 R. Tang, L. Zhou, Y. Dai, Y. Wang, Y. Cai and T. Chen, *et al.*, Polydopamine modified by pillar[5]arene in situ for targeted chemo-photothermal cancer therapy, *Chem. Commun.*, 2024, **60**(9), 1160–1163.
9 Y. Tian, M. R. Younis, Y. Tang, X. Liao, G. He and S. Wang, *et al.*, Dye-loaded mesoporous polydopamine nanoparticles for multimodal tumor theranostics with enhanced immunogenic cell death, *J. Nanobiotechnol.*, 2021, **19**(1), 365.
10 H. Xu, J. Ling, H. Zhao, X. Xu, X. K. Ouyang and X. Song, In vitro Antitumor Properties of Fucoidan-Coated, Doxorubicin-Loaded, Mesoporous Polydopamine Nanoparticles, *Molecules*, 2022, **27**(23), 8455.
11 H. Wang, D. Jia, D. Yuan, X. Yin, F. Yuan and F. Wang, *et al.*, Dimeric Her2-specific affibody mediated cisplatin-loaded nanoparticles for tumor enhanced chemo-radiotherapy, *J. Nanobiotechnol.*, 2021, **19**(1), 138.
12 C. F. Thorn, C. Oshiro, S. Marsh, T. Hernandez-Boussard, H. McLeod and T. E. Klein, *et al.*, Doxorubicin pathways: pharmacodynamics and adverse effects, *Pharmacogenet. Genomics*, 2011, **21**(7), 440–446.
13 F. Yang, S. S. Teves, C. J. Kemp and S. Henikoff, Doxorubicin, DNA torsion, and chromatin dynamics, *Biochim. Biophys. Acta*, 2014, **1845**(1), 84–89.
14 M. Kciuk, A. Gielecińska, S. Mujwar, D. Kołat, Ż. Kałuzińska-Kołat and I. Celik, *et al.*, Doxorubicin-An Agent with Multiple Mechanisms of Anticancer Activity, *Cells*, 2023, **12**(4), 659.
15 J. Fucikova, O. Kepp, L. Kasikova, G. Petroni, T. Yamazaki and P. Liu, *et al.*, Detection of immunogenic cell death and its relevance for cancer therapy, *Cell Death Dis.*, 2020, **11**(11), 1013.
16 J. Zielonka, J. Joseph, A. Sikora, M. Hardy, O. Ouari and J. Vasquez-Vivar, *et al.*, Mitochondria-Targeted Triphenylphosphonium-Based Compounds: Syntheses, Mechanisms of Action, and Therapeutic and Diagnostic Applications, *Chem. Rev.*, 2017, **117**(15), 10043–10120.
17 L. Zhang, P. Yang, R. Guo, J. Sun, R. Xie and W. Yang, Multifunctional Mesoporous Polydopamine With Hydrophobic Paclitaxel For Photoacoustic Imaging-Guided Chemo-Photothermal Synergistic Therapy, *Int. J. Nanomed.*, 2019, **14**, 8647–8663.
18 T. A. Henderson and L. D. Morries, Near-infrared photonic energy penetration: can infrared phototherapy effectively reach the human brain?, *Neuropsychiatr. Dis. Treat.*, 2015, **11**, 2191–2208.
19 J. Nam, S. Son, L. J. Ochyl, R. Kuai, A. Schwendeman and J. J. Moon, Chemo-photothermal therapy combination elicits anti-tumor immunity against advanced metastatic cancer, *Nat. Commun.*, 2018, **9**(1), 1074.
20 Y. Wang, R. Tang, D. Wang, J. Wang, Y. Huang and Y. Ding, *et al.*, Platinum(II)-Metallaclip-Based Theranostics for Cell Imaging and Synergetic Chemotherapy-Photodynamic Therapy, *Inorg. Chem.*, 2023, **62**(5), 1786–1790.
21 R. Tang, Y. Ye, S. Zhu, Y. Wang, B. Lu and Y. Yao, Pillar[6]-arenes: From preparation, host-guest property to self-assembly and applications, *Chin. Chem. Lett.*, 2023, **34**(3), 107734.
22 C. Chen, S. Zhao, A. Karnad and J. W. Freeman, The biology and role of CD44 in cancer progression: therapeutic implications, *J. Hematol. Oncol.*, 2018, **11**(1), 64.
23 H. S. Qhattal and X. Liu, Characterization of CD44-mediated cancer cell uptake and intracellular distribution of hyaluronan-grafted liposomes, *Mol. Pharm.*, 2011, **8**(4), 1233–1246.
24 B. B. Karakocak, J. Liang, P. Biswas and N. Ravi, Hyaluronate coating enhances the delivery and biocompatibility of gold nanoparticles, *Carbohydr. Polym.*, 2018, **186**, 243–251.
25 S. Elmore, Apoptosis: a review of programmed cell death, *Toxicol. Pathol.*, 2007, **35**(4), 495–516.
26 T. K. Attwood, D. B. Kell, P. McDermott, J. Marsh, S. R. Pettifer and D. Thorne, Utopia documents: linking scholarly literature with research data, *Bioinformatics*, 2010, **26**(18), i568–i574.
27 L. Jiang, H. Yu, C. Wang, F. He, Z. Shi and H. Tu, *et al.*, The Anti-Cancer Effects of Mitochondrial-Targeted Triphenylphosphonium-Resveratrol Conjugate on Breast Cancer Cells, *Pharmaceuticals*, 2022, **15**(10), 1271.

28 S. Sivagnanam, K. Das, I. Pan, A. Stewart, A. Barik and B. Maity, *et al.*, Engineered triphenylphosphonium-based, mitochondrial-targeted liposomal drug delivery system facilitates cancer cell killing actions of chemotherapeutics, *RSC Chem. Biol.*, 2024, **5**(3), 236–248.
29 M. P. Murphy, How mitochondria produce reactive oxygen species, *Biochem. J.*, 2009, **417**(1), 1–13.
30 S. Rius-Pérez, S. Pérez, M. B. Toledano and J. Sastre, Mitochondrial Reactive Oxygen Species and Lytic Programmed Cell Death in Acute Inflammation, *Antioxid. Redox Signaling*, 2023, **39**(10–12), 708–727.
31 J. Xu, W. Du, Y. Zhao, K. Lim, L. Lu and C. Zhang, *et al.*, Mitochondria targeting drugs for neurodegenerative diseases-Design, mechanism and application, *Acta Pharm. Sin. B*, 2022, **12**(6), 2778–2789.
32 K. B. Wallace, V. A. Sardão and P. J. Oliveira, Mitochondrial Determinants of Doxorubicin-Induced Cardiomyopathy, *Circ. Res.*, 2020, **126**(7), 926–941.

